



HAL
open science

On the high cycle fatigue resistance of austenitic stainless steels with surface gradient microstructures: Effect of load ratio and associated residual stress modification

Clément Dureau, Mandana Arzaghi, Roxane Massion, Yves Nadot, Thierry Grosdidier

► **To cite this version:**

Clément Dureau, Mandana Arzaghi, Roxane Massion, Yves Nadot, Thierry Grosdidier. On the high cycle fatigue resistance of austenitic stainless steels with surface gradient microstructures: Effect of load ratio and associated residual stress modification. *Materials Science and Engineering: A*, 2022, pp.142916. 10.1016/j.msea.2022.142916 . hal-03601305

HAL Id: hal-03601305

<https://hal.univ-lorraine.fr/hal-03601305v1>

Submitted on 9 Mar 2022

HAL is a multi-disciplinary open access archive for the deposit and dissemination of scientific research documents, whether they are published or not. The documents may come from teaching and research institutions in France or abroad, or from public or private research centers.

L'archive ouverte pluridisciplinaire **HAL**, est destinée au dépôt et à la diffusion de documents scientifiques de niveau recherche, publiés ou non, émanant des établissements d'enseignement et de recherche français ou étrangers, des laboratoires publics ou privés.

1 **On the high cycle fatigue resistance of austenitic stainless steels with surface gradient**
2 **microstructures: effect of load ratio and associated residual stress modification**

3

4 Clément DUREAU^{1,2,3}, Mandana ARZAGHI³, Roxane MASSION^{1,2}, Yves NADOT³, Thierry
5 GROSDIDIER^{1,2*}

6 ¹ Université de Lorraine, Laboratoire d'Etude des Microstructures et de Mécanique des Matériaux, CNRS
7 UMR 7239, 7 rue Félix Savart, 57073 Metz, France

8 ² Université de Lorraine, LABoratoire d'EXcellence Design des Alliages Métalliques pour Allègement de
9 Structures, 7 rue Félix Savart, 57073 Metz, France

10 ³ Institut Pprime, UPR 3346 CNRS- ISAE-ENSMA- Université de Poitiers, Téléport 2, 1 Avenue Clément
11 Ader, BP 40109, 86961 Futuroscope Chasseneuil Cedex

12 *Corresponding author: Thierry GROSDIDIER thierry.grosdidier@univ-lorraine.fr

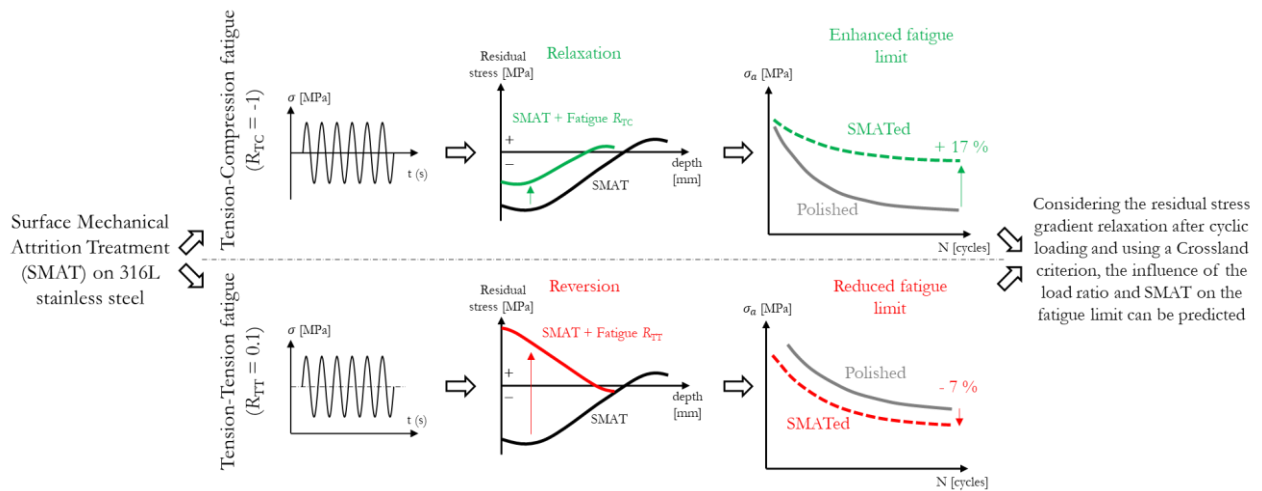
13 **Abstract**

14 The effect of gradient microstructure generated by ultrasonic surface mechanical attrition treatment (SMAT)
15 on the fatigue performance of an austenitic stainless steel has been evaluated in the context of localized and
16 general plasticity by comparing two load ratios: fully reversed tension-compression (TC) $R_{TC} = -1$ and
17 tension-tension (TT) $R_{TT} = +0.1$, respectively.

18 After identical SMAT processing conditions, the fatigue limit was enhanced by +17 % for R_{TC} while it was
19 reduced by -7 % for R_{TT} . Under R_{TC} cyclic loading, self-heating of the specimens and sub-surface martensitic
20 transformation occurred but not for R_{TT} . The residual stress measurements have also revealed that while the
21 stress gradient was smoothed after the R_{TC} fatigue loading, it was completely reverted for the R_{TT} one. In turns,
22 the fatigue crack initiation sites and propagation were modified between the R_{TT} and R_{TC} loading conditions.

23 Considering the stabilized surface residual stress after fatigue loading, the use of a Crossland criterion allowed
24 to explain both the effects of load ratio and SMAT on the high cycle fatigue behavior of the stainless steel. It
25 turns out that under the studied loading conditions the modifications of residual stress state can be considered
26 as the primary factor governing the varying fatigue performances and the observed triggering at different
27 initiation sites.

28 **Graphical abstract**



29

30 **Keywords:** Surface mechanical attrition treatment (SMAT), ultrasonic shot peening (USP), 316L austenitic
31 stainless steel, fatigue, load ratio, residual stresses

32 **1. Introduction**

33 In the last two decades, functionally graded materials (FGMs) have been broadly studied, particularly
34 those with varying properties from surface to core. In addition, such materials offer unique mechanical or
35 chemical properties through microstructure or hardening gradients. As a result, automotive, aeronautic, or
36 energy production industries expect them to produce higher efficiency and more reliable components [1, 2],
37 especially those subjected to fatigue issues.

38 In cases such as corrosion, friction wear, or fatigue for which the surface is a critical issue, surface
39 modifications may be sufficient to improve the properties of the mechanical part. In terms of fatigue, as most
40 cracks initiate from the surface, inducing a compressive residual stress state by shot peening improves the
41 fatigue limit of a wide variety of materials [3-7]. Also, surface severe plastic deformation (SPD) processes that
42 lead to FGMs having an ultrafine grain (UFG) surface microstructure represent a way to enhance the functional
43 properties of materials. Among those processes, surface mechanical attrition treatment (SMAT) or ultrasonic
44 shot peening (USP) are derived from conventional shot peening (CSP) [8-12]. They differ from CSP because
45 the motion of the shots is made within a confined chamber so that the shots can impact the surface of the
46 sample, by colliding and bouncing on the chamber walls, for a potentially longer time and with a wider range
47 of incidence angles. This leads to an increased number of activated slip systems allowing to very effectively
48 refine the microstructure leading to a UFG state at the surface and the formation of a gradient

49 microstructure [13, 16]. SMAT or similar treatments were suggested to be efficient ways to enhance the fatigue
50 behavior of many metallic alloys due to the coupled effect of microstructure, hardening gradient, and
51 compressive residual stresses [17-22]. However, some manuscripts suggested that SMAT can be detrimental
52 for some materials or if the chosen set of parameters for the SMAT treatment is not optimized [23-27].

53 The 316L stainless steel is an example of highly used austenitic steel that, despite its good oxidation
54 and corrosion resistances as well as its good formability, suffers from moderate mechanical properties.
55 Different strengthening processes have been studied as a way to improve the mechanical properties of such
56 alloys without giving up too much of their other characteristics [28-30]. By inducing hardening, residual
57 stresses, and UFG microstructure layer, SMAT or similar processes have also been suggested to improve the
58 fatigue behavior of 316L stainless steel. Indeed, Masaki et al. measured a nearly 100 % increase of the fatigue
59 limit of 316L samples after hard shot-peening (HSP) when loaded in rotating bending [31]. Uusitalo et al. [18]
60 and Roland et al. [32] respectively observed an 83 % and 21 % higher fatigue limit after performing SMAT
61 with 3 mm diameter beads on 316L. Comparatively, with similar SMAT treated 316L samples, Sun et al.
62 highlighted that the number of cycles to failure was unchanged compared to the untreated ones in the low cycle
63 fatigue (LCF) regime despite the enhanced stress amplitudes for the SMAT-processed specimens [33]. Here
64 again, on austenitic stainless steels, the literature gives apparently conflicting results. This unchanged fatigue
65 life was proposed to be due to the higher residual stress relaxations induced by the higher strain amplitudes in
66 LCF than in high cycle fatigue (HCF). This was then further investigated by Sun et al., who reported an almost
67 fully relaxed residual stress gradient after a fatigue test conducted at 1.25 % of strain amplitude [34].
68 Huang et al. even measured a slight tensile residual stresses gradient after 3 % strain [35]. Therefore, this
69 suggests that the macroscopic plastic strains could be affecting the residual stress gradient relaxation after
70 fatigue loading, and then the fatigue life of SMAT processed samples. But, most of the fatigue testing available
71 in the literature [30, 32, 35] have been conducted in fully reversed loading condition ($R = -1$), and as in this
72 configuration the measured fatigue limits were in the same range of magnitude as the yield strength of the
73 material, no data about the effect of macroscopic strain on the HCF behavior of SMAT processed 316L are
74 available.

75 Thus, the goal of the present work is to shed some light on the exact capability of the SMAT to enhance
76 the high cycle fatigue behavior for different loading conditions by taking the well-known commercial 316L
77 stainless steel as a good test subject. Special attention will be paid to the effect of surface roughness and, as the

78 applied load ratio directly influences the macroscopic strains, to the evolutions of hardness and residual stress
79 redistributions after fatigue loading.

80 2. Materials and Methods

81 2.1. Sample preparation and surface treatment

82 The studied material was an AISI 316L stainless steel formed by swaging above 1040 °C into a 20 mm
83 diameter bar. Table 1 summarizes the chemical composition of this steel together with the resulting martensite
84 start temperature M_S and the M_{d30} temperature at which 50 % of martensite is formed when the material is
85 subjected to a 30 % true strain. A heat treatment of 40 min at 900 °C was done on this raw material, resulting
86 in a homogeneous microstructure with an average grain size of approximately 30 μm . Tensile tests revealed a
87 yield stress $\sigma_{ys} = 220$ MPa, an ultimate tensile stress $\sigma_{UTS} = 650$ MPa and an elongation to failure of 105 %.
88 Fatigue specimens with a 9 mm diameter and a 12.5 mm gauge length were machined. In order to remove the
89 plastically deformed and heat-affected zone induced by machining, a layer of about 75 μm was removed by
90 grinding the samples before polishing them to a mirror finish surface. While half of the polished samples were
91 kept in this condition (initially polished condition – Table 2 a), the other half was treated by SMAT (SMAT
92 condition – Table 2 a). The treatment was carried at a hitting distance of 20 mm for 60 min using a SONATS
93 ultrasonic shot peening device [36] equipped with a sonotrode made of Ti-6Al-4V that was vibrating at a 60 μm
94 amplitude and a 20 kHz frequency. A total of 4.1 grams of brand new 2 mm diameter 100C6 beads were
95 inserted in the dedicated polyoxymethylene chamber before each treatment and two samples were treated
96 simultaneously. The samples were rotated at a speed of 20 revolutions per minute during this surface
97 mechanical attrition treatment. For specific analysis that will be described later on, some of these SMATed
98 samples were mirror polished after a delicate grinding procedure with 1000 grit SiC abrasive
99 paper (SMAT + polished condition – Table 2 a), resulting in a removed thickness of approximately 35 μm . All
100 the above-mentioned surface conditions are gathered in Table 2 a with their respective surface roughness.

101 2.2. Fatigue tests

102 The fatigue tests were load-controlled to evaluate the overall HCF performance of the studied material
103 for different load ratios. The load ratio is defined by Equation (1), and in order to study its effect on the uniaxial
104 fatigue behavior of the polished and SMAT states of the 316L stainless steel, both tension-compression (TC)
105 and tension-tension (TT) fatigue tests were conducted.

106
$$R = \sigma_{\min} / \sigma_{\max} \quad (1)$$

107 The following values of the load ratio were selected: $R_{TC} = -1$ and $R_{TT} = +0.1$. The fatigue tests were carried out
108 at room temperature at a loading frequency of 10 Hz with an 810MTS servo-hydraulic machine. Any sample
109 reaching 10^6 cycles without breaking was considered a run-out and was not reused.

110 2.3. Samples characterization

111 Fracture surfaces of the broken samples were analysed using optical microscopy (OM) and scanning
112 electron microscopy (SEM) to reveal the differences in crack initiation and propagation between the different
113 tested conditions.

114 In order to decorrelate the influence of the gradients of microstructure, hardness, and residual stresses,
115 reference SMATed samples were compared to the run-out samples that experienced the highest fatigue tested
116 stress amplitude under R_{TC} and R_{TT} without failure. They were denominated as “SMAT + Fat R_{TC} ” and
117 “SMAT + Fat R_{TT} ”. A final condition was studied, for which a SMATed sample was tested for one single cycle
118 at R_{TT} at the same stress level as the SMAT + Fat R_{TT} one. This sample was analysed to learn about the effect
119 of the number of fatigue cycles; it was named “SMAT + 1Cy R_{TT} ”. The testing conditions and their labelling
120 are gathered in Table 2 b. For these four conditions (SMAT, SMAT + Fat R_{TC} , SMAT + Fat R_{TT} and
121 SMAT + 1Cy R_{TT}), the hardening state characterization was done by standard HV 0.3/20 Vickers micro-
122 hardness measurements. They were conducted on specimen cross sections perpendicularly to the SMAT layer
123 starting 30 μm below the surface until reaching the core material. Each indent was spaced by 100 μm to avoid
124 interference, and 10 measurements were conducted for each given depth. In parallel, the in-depth residual stress
125 gradients before and after fatigue loading of those four samples were characterized by X-ray diffraction after
126 successive material layer removal using electrochemical polishing. For electro-polishing, a solution consisting
127 of a mix of 6 % perchloric acid, 35 % butoxyethanol and 59 % methanol was used. The cylindrical fatigue
128 samples were rotated during the XRD measurement to increase the number of diffracting grains and average
129 potential local effects. A Pulstec μ -X360s device with a mounted Cr tube operating at 30 kV and 1.5 mA
130 allowed to obtain full diffraction rings from the two-dimensional detector. The “Analysis Tools for Electron
131 and X-ray diffraction” (ATEX) software [37], developed in LEM3, was used for post-processing the acquired
132 data using the “cos α ” method. Finally, due to the residual stress redistribution occurring during successive
133 material layer removal, the experimentally measured gradient was corrected using the Moore and Evans
134 relations [38].

135 3. Results

136 The results will be presented hereafter into different subsections. The first subsection gathers the
137 fatigue test results. Fatigue tests were carried out at R_{TC} for both the polished and SMAT conditions to set the
138 reference data for easier comparison with the literature. Then similar tests were conducted at R_{TT} in order to
139 highlight the effect of the load ratio. The second subsection details the analysis of the fracture surfaces. The
140 third subsection deals with the analysis of the run-out samples. First, the surface of the run-out samples were
141 investigated using SEM to look for potential fatigue cracks. Also, residual stress as well as hardness evolutions
142 were studied to get further information about the material behavior in the fatigue limit regime of the SMATed
143 samples for both R_{TC} and R_{TT} . Finally, this result section will be concluded by a Crossland initiation criterion
144 analysis taking into account the relaxed residual stress fields to analyse the combined effects of load ratio and
145 SMAT.

146 3.1. Fatigue properties

147 Figure 1 gives the Wöhler curves obtained for the polished and the SMAT conditions for both testing
148 conditions: TC in Figure 1 a and TT in Figure 1 b. Circles represent the polished samples while the squares
149 and stars the SMAT and SMAT + polished conditions, respectively. The full and hollow symbols indicate the
150 broken and run-out specimens, respectively. The experimental data were fitted using the Stromeier
151 equation [39] defined by Equation (2), a full line was used for fitting the polished state and a dotted line for the
152 SMAT one, while the SMAT + polished data were not fitted due to the small number of tested specimens.

$$153 \quad \sigma_a = \sigma_D + \left(\frac{c}{N}\right)^{1/m} \quad (2)$$

154 In Figure 1 a, the results obtained by Dureau et al. in a previous study on the 304L stainless steel [40] were
155 superimposed. Indeed, the data reported in Figure 1 a show that the 304L and 316L samples exhibit very
156 similar fatigue behavior for both surface conditions.

157 For the Wöhler curves of the samples loaded at R_{TC} (Figure 1 a), the fatigue limits are estimated to be
158 205 MPa and 240 MPa for the polished and SMAT conditions, respectively. Clearly, the SMAT provided an
159 increase of about +17 % of the fatigue limit at R_{TC} . For this R_{TC} loading condition, self-heating of the surface
160 of the specimens as high as 150 and 250 °C was measured for the highest tested stress amplitudes for the
161 polished and SMATed samples respectively. For the samples loaded in the range of the fatigue limit, the
162 self-heating was less than 50 °C and considered negligible, similarly to what was reported in a previous

163 work [40]. For the R_{TT} loading, Figure 1 b indicates that the fatigue life of the SMATed samples was very
164 similar to the polished ones in the 10^5 cycle regime, while it tended to be slightly lower in the 10^6 cycle domain.
165 Under R_{TT} , the fatigue limits were estimated to be 230 MPa and 215 MPa for the polished and SMAT
166 conditions, respectively. Comparatively, for the SMAT + polished specimens also loaded at R_{TT} , the fatigue
167 life as well as the fatigue limit of those specimens appeared to be slightly increased compared to the SMATed
168 ones due to the post-polishing procedure. Contrary to what was observed for the R_{TC} condition, a reduction of
169 about -7 % is induced by the surface mechanical attrition treatment when the samples are loaded at R_{TT} . The
170 initially polished and SMAT + polished data almost superimpose for the R_{TT} conditions. This indicates that the
171 actual surface state has an influence since the post-polishing procedure restored the overall fatigue properties.
172 Interestingly, contrary to what was reported at R_{TC} , no self-heating of the specimens was measured for this load
173 ratio.

174 3.2. Broken samples analysis

175 Figure 2 presents typical SEM images of the characteristic initiation sites observed on the different
176 tested specimens. In Figure 2, the three horizontal lines correspond to the surface state of the samples (initial
177 polished, SMAT, or SMAT + polished) while the columns rank the observations made for the two load ratios,
178 R_{TC} or R_{TT} , with images of samples that broke under high or low stress amplitudes.

179 For the R_{TC} loaded samples, the comparative analysis of the fracture surfaces - at a given stress
180 amplitude for the polished and SMAT conditions - revealed very similar fatigue crack initiation features. As
181 marked by the red arrows in Figure 2 a1, the high stress amplitude is witnessed by the presence of a secondary
182 crack intercepting the fracture surface in the vicinity of the initiation site of the polished sample. For the SMAT
183 samples subjected to a high stress amplitude, as illustrated in Figure 2 b1, no such crack was observed; instead,
184 a very distinct river line aspect was revealed. For the low stress amplitude conditions, as shown in Figures 2 a2
185 and b2, no difference was noticed on the initiation sites regardless of the surface condition. Thus, the observed
186 modification of the crack initiation was more influenced by the applied stress amplitude than by the exact
187 nature of the surface.

188 For the samples loaded at R_{TT} at high stress amplitudes, all the samples experienced fatigue crack
189 initiation on surface inclusions whatever the exact nature of the surface condition as seen in Figures 2 c1, d1
190 and e1. Moreover, all the observed inclusions exhibited a rather circular shape except for the SMAT conditions.
191 Indeed, compared to the round solid inclusion shown in Figure 2 c1 for the polished sample, the inclusion seen

192 in Figure 2 d1 for the SMAT sample exhibits numerous sharp angles and facets. Indeed, in the case of rather
193 large particles located at or just beneath the surface, the repeated impacts can result in their fragmentation
194 directly under the action of SMAT. This can explain why fragmented inclusions were observed in some SMAT
195 samples (Figure 2 d1) but not in the polished ones (Figure 2 c1). Figures 2 e1 highlights, once again, an
196 initiation on a surface solid inclusion for the SMAT + polished condition; even if the inclusion was even ejected
197 from the fracture surface for this specific sample, leaving a cavity. For the lowest stress amplitudes, initiation
198 also occurred at the surface for the three conditions. However, inclusions were never observed at the initiation
199 site of the analysed initial polished and SMAT conditions. Figure 2 c2 demonstrates that, as no inclusion is
200 found, fatigue cracks are probably initiated on surface roughness induced by plasticity such as slip bands. In
201 contrast, Figure 2 d2 shows that for the SMAT, initiation occurred on a dimple (i.e., a surface asperity induced
202 by SMAT), as will be confirmed in Figure 3. For the SMAT + polished samples loaded at low
203 stress (Figure 2 e2), initiation occurred at a surface inclusion as previously described for the R_{TT} high stress
204 conditions. However, due to the lower number of tested samples, it seems speculative to conclude that no
205 change in the initiation mechanism is observed when reducing the stress amplitude in the case of
206 SMAT + polished samples.

207 Figure 3 gathers the EDX maps corresponding to the four areas surrounded by red rectangles in
208 Figure 2. Only the case of R_{TT} samples is presented because the analysis carried out on the initiation sites of
209 the R_{TC} samples did not reveal any inclusion or chemical heterogeneity. As shown in Figure 3 a, the inclusion
210 found at the initiation site of the polished sample loaded at high stress amplitude is a rather complex calcium-
211 aluminate oxide also containing magnesium. The inclusion visible in Figure 2 e2 for the case of a low stress
212 SMAT + polished sample loaded at R_{TT} was another calcium aluminate oxide containing magnesium and
213 silicon. The inclusions could also be simple aluminium oxides, as shown in Figure 3 b for a SMAT sample
214 loaded at high amplitude. The most probable explanation for the presence of these different oxides is that they
215 are initially formed between the molten metal and the slag by the addition of deoxidation products during the
216 argon oxygen decarburation process. As explained by Zhang et al. [41], this usually leads to the formation of
217 characteristic oxides based on SiO_2 , CaO , and Al_2O_3 . These oxides being solid in the molten metal due to their
218 higher melting temperature, they are present in the final product as inclusions of different oxide chemistry.
219 These observed inclusions have a fairly nodular shape with a diameter of about 10 μm regardless of their
220 composition. On the other hand, Figure 3 c reveals that the dimple defect observed in Figure 2 d2 is filled by
221 aluminium, titanium, and vanadium. This chemical composition corresponds to the characteristic

222 contamination layer that can form during sufficiently long surface mechanical attrition treatment. Such type of
223 contamination layer is known to form by erosion ablated scraps coming from the 100C6 shots, the Ti-6Al-4V
224 sole of the sonotrode or even particles from the chambers. Such contamination layer was already observed by
225 Samih et al. and was even shown to reach depths of approximately 5 μm due to the pile-up, ablation, and
226 deposition mechanisms for similar SMAT conditions [42]. These observations were later confirmed by
227 Chemkhi et al. on SMATed 316L stainless steel [43]. This contamination layer is known to affect the reactivity
228 and corrosion resistance of the SMAT treated surfaces [10]. Its chemistry was also shown to have determining
229 consequences regarding the wear behavior of the shot peened surfaces due to its effect on the exact nature of
230 the abrasive oxides that form during dry contact friction [44].

231 Figure 4 compares the macroscopic optical observations of the fracture surfaces of the different tested
232 specimen conditions (line a) with sketches of the fracture sequence with topology of these fracture surfaces
233 (line b). For the R_{TT} loading conditions, the observed features for the SMAT and the SMAT + polished samples
234 were similar; thus, only the SMAT condition is shown. For the R_{TC} loading condition of the polished sample
235 (Figure 4 a1), the observation shows a fairly straight propagation front perpendicular to the propagation
236 direction (i.e., sample radius) before the final fracture. Comparatively, the propagation region forms an internal
237 circular-like area for the SMAT samples (Figure 4 a2). The same behavior was observed in a previous study
238 on a 304L stainless steel treated by SMAT and loaded at R_{TC} [40]. For the R_{TT} loading conditions (Figure 4 a3
239 and a4), semi-circular crack fronts were observed before the occurrence of a ductile fracture for all conditions.
240 At this scale, no obvious difference in the shape of the fracture surfaces was observed when comparing the
241 different polished and SMAT samples loaded at R_{TT} . Figures 4 b1, b2, b3, and b4, give the topology of the
242 fracture surfaces and the initiation site was taken as the reference point for the measured altitude. The
243 propagation plateau in the case of the R_{TC} polished sample is perfectly perpendicular to the loading axis, as
244 indicated in Figure 4 b1 by the large domain of blue colour pointed by the red arrow. Comparatively, in the
245 central region of the fracture surface of the R_{TC} SMAT sample, a slight angle of about 7° was observed
246 perpendicular to the crack propagation direction due to the higher stress amplitude, as shown in Figure 4 b2.
247 In addition as indicated by the dotted black arrows, the fatigue fracture surface delimited by the circle-like
248 dotted line in Figure 4 b2 continued toward the hardened surface by a propagation zone inclined at 45° . Minor
249 differences can be noticed on the fracture surfaces when comparing the R_{TT} conditions (Figures 4 b3 and b4).
250 However, inclined propagation zones are visible in the vicinity of the surface for the shot peened samples, as
251 outlined in Figure 4 b4 by the regions delimited by the curved dotted lines and pointed by the red arrows. These

252 specific crack propagation features for the SMAT samples loaded at R_{TC} and R_{TT} , because they were not visible
253 for the initial polished samples, are then linked to the presence of the SMAT affected layer. They can either
254 result from the microstructure and especially texture effects, as was already discussed for several UFG metallic
255 materials such as interstitial-free steel [45], aluminium alloy [46], or commercially pure copper [47]. As the
256 texture modifications under SMAT are rather weak [48], the modifications in crack propagation are more likely
257 due to the tri-axial field of residual stress generated in this region. It leads to a curved crack propagation path,
258 as discussed by Cotterell and Rice [49]. As shown by comparing Figures 4 b1, b2, b3, and b4, the failure
259 sequence always consists of three stages. For all conditions, it starts with a surface crack initiation followed by
260 a propagation phase and finishes with a ductile fracture. However, as confirmed by the larger domains of grey
261 contrast in Figures 4 b3 and b4, the ductile fracture occurred after much shorter fatigue crack propagation for
262 the R_{TT} than for the R_{TC} ones (Figures 4 b1 and b2). This is expected since, for an identical stress amplitude,
263 the maximum macroscopic stress is more than twice as high for the R_{TT} loading condition than for the R_{TC} one.
264 Also, due to this much higher stress while breaking, samples loaded at R_{TT} experienced necking and bending,
265 leading to a much more deformed final section (Figures 4 b3 and b4) compared to the R_{TC} samples for which
266 the original circular section can still be clearly distinguished (Figures 4 b1 and b2).

267 3.3. Unbroken samples analysis

268 Figure 5 presents the characteristic surface state of the run-out samples observed by SEM. ~~For R_{TC} the~~
269 ~~images are not presented because, for the polished samples, the observation only revealed fine witness marks~~
270 ~~of plastic activity while, for the SMAT samples, observation was nearly impossible due to the roughness of the~~
271 ~~surface and the presence of the contamination layer (previously discussed in Figure 3 e) partially covering the~~
272 ~~sample surface.~~ For R_{TC} , Figure 5 a reveals fine witness marks of plastic activity visible on the polished
273 surface. Some favourably oriented grains exhibit slip bands which usually are parallel. Such traces were not
274 visible for the SMAT samples (Figure 5 b) due to the roughness of the surface and the presence of the
275 contamination layer (previously discussed in Figure 3 c) partially covering the sample surface. For R_{TT} , as
276 shown in Figure 5 c, the surface of the polished samples is very affected by the fatigue loading. Indeed, it is
277 covered with highly pronounced slip bands and the deformation of the grains creates a micro-roughness leading
278 to the classic “orange-peel” aspect of the deformed samples. For the R_{TT} loaded SMAT samples, Figure 5 d
279 illustrates that the contamination layer covering the SMAT sample surface is not homogeneous. Indeed, in
280 Figure 5 d, the yellow dashed curve delimits the left end side where the rough surface of the fatigue sample is
281 visible from the right end side where the contamination layer appears in a darker colour. Once again, the rough

282 SMAT surface does not allow to identify surface plasticity. Comparatively, as indicated by the red arrows, it
283 is interesting to notice that the contamination layer of the samples has fractured during the fatigue loading due
284 to the elongation of the stainless steel substrate. For the SMAT + polished condition, slip bands are visible at
285 the surface of the samples (Figure 5 e). However, due to the refined microstructure generated during SMAT,
286 the slip bands are not as straight as for the initial polished state. Figure 5 has shown that different surface states
287 and plastic activity were identified for the different studied conditions. Nevertheless, fatigue crack initiation
288 was never detected for run-out samples regardless of their surface condition or the imposed stress amplitude
289 and load ratio. This indicates that initiation seems to be the key aspect to consider when studying the effect of
290 SMAT on the HCF behavior of stainless steel.

291 Figure 6 gives the evolutions of the longitudinal component of the residual stress tensor with respect
292 to the depth below the surface for different conditions. Figure 6 a compares the stress gradient after fatigue on
293 a run-out sample for the R_{TC} loading (SMAT + Fat R_{TC} condition for $\sigma_a = 240$ MPa) with the reference SMAT
294 one. Figure 6 b shows the evolutions of the stress state for R_{TT} loading after one cycle (SMAT + 1Cy R_{TT} for
295 $\sigma_a = 215$ MPa) and after another fatigue run-out (SMAT + Fat R_{TT} also for $\sigma_a = 215$ MPa). The reference
296 SMAT sample characterization is presented by solid black curves, while dotted and dashed lines are used after
297 loading. As the 316L stainless steel samples underwent stress- or strain-induced martensitic phase
298 transformation during the SMAT process, two phases did coexist. Thus, in the graphs, circles are the measured
299 values of residual stress in austenite (γ), while squares are used for martensite (α'). The error bars represent
300 the standard deviation of each linear fit used in the “cos α ” method for each measured point. For clarity, they
301 are only displayed when the standard error is more than 50 MPa. As shown by the solid black curves in
302 Figures 6 a and b, SMAT allowed to create a compressive residual stress gradient along about 600 μm below
303 the treated surface. Due to the stress and strain fields, a partial martensitic transformation occurred in the first
304 100 μm below the surface. This is rather consistent with the observations of Novelli et al. on the 304L stainless
305 steel [50], even if it has to be recalled that the austenite in the 304L is less stable and then more susceptible to
306 undergo martensitic transformation than for the 316L. For the reference SMAT condition, surface residual
307 stresses of approximately -600 MPa and -900 MPa were evaluated in austenite and martensite, respectively.
308 The maximum values of residual stresses were recorded slightly below the surface. They were -750 MPa for
309 austenite at 100 μm below the surface and -1 GPa for martensite at a depth of 25 μm . These results are
310 consistent with observations made by different authors [34, 40, 51]. Interestingly, after fatigue, stress
311 relaxation took place in very different ways depending on the loading conditions. As shown in Figure 6 a for

312 the R_{TC} loading, the surface stresses were relaxed by approximately 50 % in both austenite and sub-surface
313 martensite for the SMAT + Fat R_{TC} sample. This resulted in approximately constant internal stress levels along
314 the first 100 μm below the surface with values of -250 MPa and -500 MPa in the austenite and martensite
315 phases, respectively. In addition to this compressive residual stress relaxation, the depth of the gradient was
316 also reduced down to 275 μm . Moreover, it is very interesting to notice that additional martensite was created
317 during the cyclic loading at depths below 200 μm (down to about 350 μm because deeper investigations were
318 not conducted). Thus, due to the load condition of SMAT followed by fatigue at R_{TC} , martensite was present
319 in a fair amount at depth in the range 0-100 μm and below 200 μm but not detected in the 100-200 μm depth
320 domain. For the R_{TT} loading conditions, a reversion of the residual stress state was revealed. Indeed, for the
321 SMAT + Fat R_{TT} sample, surface stresses of +850 MPa and +1250 MPa were measured in austenite and
322 martensite, respectively. Similarly to what was observed on the SMAT + Fat R_{TC} , the residual stresses stored
323 in martensite were relatively constant but, in this case, no additional stress- or strain-induced martensite was
324 formed in the subsurface. In austenite, the internal stress level decreased almost linearly as a function of depth
325 down to 350 μm below the surface. Interestingly, the stress gradient was almost completely reverted after only
326 one cycle of R_{TT} fatigue. Indeed, surface stress of +750 MPa in austenite and +1150 MPa in martensite were
327 measured for the SMAT + 1Cy R_{TT} sample.

328 Figure 7 compares the SMAT reference hardness gradient with the ones measured after the different
329 loading conditions. Figures 7 a, b, and c present the results for the SMAT + Fat R_{TC} , SMAT + Fat R_{TT} , and
330 SMAT + 1Cy R_{TT} samples, respectively. Each point represents the average value and the error bars are the
331 minimum and maximum hardness values measured at the corresponding depth. The hardness gradient for the
332 reference SMAT sample before fatigue is displayed in every graph. It is characterized by a maximum value of
333 500 HV measured 50 μm below the surface and an estimated total hardened layer of about 600 μm . These
334 values are consistent with data from the literature on the 316L and 304L alloys after comparable surface
335 mechanical attrition treatments [34, 40, 52, 53]. After cyclic loading for one cycle or more, the curves of the
336 SMAT + Fat R_{TC} , SMAT + Fat R_{TT} , and SMAT + 1Cy R_{TT} samples depict a general gradient evolution that is
337 quite similar to the reference SMAT one. However, when sufficient fatigue cycles were applied (i.e., for the
338 two SMAT + Fat conditions in Figures 7 a and b), a slight softening was detected at the subsurface
339 between 100 and 200 μm (as indicated by the single red arrows), while, as pointed by the double red arrows
340 below 600 μm , a hardening was measured in the so-called “core material”. Differences in the behavior of
341 dislocations can explain these two opposite phenomena. Indeed, during cyclic loading, the annihilation of

342 dislocations created under SMAT occurs, thus leading to softening in the subsurface. Similar explanation was
 343 given in the work of Sun et al. in which a similar behavior was observed [33]. In the core material, new
 344 dislocations were created during fatigue, and the material was hardened. The stabilized value in the core is
 345 220 HV, which represents an increase of about 10 % compared to the initial hardness of the material. The
 346 absence of significant differences for the SMAT + 1Cy R_{TT} sample indicates that several cycles of fatigue are
 347 needed to reach the stabilized hardened state.

348 3.4. Crossland criterion

349 The fact that the residual stress gradient after fatigue was shown to be drastically different for both
 350 loading conditions (RTC and RTT) indicates that not only the macroscopic loading has to be considered to
 351 understand the influence of SMAT on the fatigue limits for those two load ratios. Moreover, as for each tested
 352 conditions the fatigue limit was shown to be characterised by the incapacity of fatigue cracks to initiate, an
 353 initiation endurance criterion taking into account the multiaxial stress field at the surface of the fatigue samples,
 354 such as the Crossland criterion [54], seems to be a way to understand the difference of effectiveness of such
 355 treatment in the HCF regime. Three hypotheses were considered to establish the Crossland criterion. The first
 356 one is that the initial polished samples were exempt from residual stress due to the surface polishing after
 357 machining. The second one is that the free surface of the SMAT samples is considered to be under a plane
 358 stress state and that the shear components σ_{12} and σ_{21} are negligible compared to the longitudinal and tangential
 359 ones σ_{11} and σ_{22} . The third one is that only the residual stress state measured in austenite was considered
 360 because the proportion of martensite was limited and not quantified in detail, so that a “rule of mixtures” could
 361 not be used. Considering that the estimated fatigue limits are $\sigma_{RTC}^{\text{polished}} = 205$ MPa, $\sigma_{RTC}^{\text{SMAT}} = 240$ MPa,
 362 $\sigma_{RTT}^{\text{polished}} = 230$ MPa, and $\sigma_{RTT}^{\text{SMAT}} = 215$ MPa, and that the stabilized surface residual stress tensors after fatigue
 363 loading of the SMAT samples are:

$$364 \quad \underline{\underline{RS}}_{RTC}^{\text{SMAT}} \begin{bmatrix} -229 & \sim 0 & 0 \\ \sim 0 & -512 & 0 \\ 0 & 0 & 0 \end{bmatrix} \quad \text{and} \quad \underline{\underline{RS}}_{RTT}^{\text{SMAT}} \begin{bmatrix} +872 & \sim 0 & 0 \\ \sim 0 & -225 & 0 \\ 0 & 0 & 0 \end{bmatrix}$$

365 The following two stress tensors invariants were calculated. $J_{1,\max} = \frac{1}{3} \text{tr}(\underline{\underline{\sigma}}_{\max})$ and $\sqrt{J_{2,a}} = \sqrt{\frac{1}{2} \underline{\underline{S}}_a : \underline{\underline{S}}_a}$
 366 where $\underline{\underline{S}}_a$ is the stress amplitude tensor deviator defined by $\underline{\underline{S}}_a = \underline{\underline{\sigma}}_a - \frac{1}{3} \text{tr}(\underline{\underline{\sigma}}_a) \cdot \underline{\underline{I}}$. The results are plotted in
 367 Figure 8 for the different load ratios and surface state conditions. The two points corresponding to the fatigue
 368 limits of the polished conditions for R_{TC} (hollow circle) and R_{TT} (filled circle) are located in a similar $\sqrt{J_{2,a}}$ area

369 of the graph due to the comparable measured fatigue limits. However, the point representing the polished R_{TT}
370 (filled circle) condition is shifted to the right on the $J_{1,max}$ axis compared to the R_{TC} (hollow circle) one due to
371 the higher maximum stress during cycle for this load ratio. Comparatively, for both SMAT conditions, the
372 residual stress state acts as a mean stress during cyclic loading. Thus, due to the compressive stress field, the
373 point corresponding to the R_{TC} SMAT condition (hollow square) is pushed in the region of the graph where
374 $J_{1,max}$ is negative. Because of the surface tensile residual stresses for R_{TT} SMAT (filled square), the
375 corresponding point is shifted to the right end side of the graph. The four points are almost aligned in a slightly
376 decreasing trend indicating the negative effect of the maximum hydrostatic pressure, which is usually observed
377 in the Crossland criterion representations [54, 55]. Moreover, the obtained fitted linear curve separates the
378 graph into two regions. The region below the curve corresponds to the “safety domain” where failure will not
379 occur. In contrast, the region above the line represents the “failure domain” in which cracking will occur, and
380 fracture of the sample should happen.

381 4. Discussions

382 The previous section has shown that the load ratio applied to a specimen has a non-negligible impact
383 on the potential effect of SMAT on the HCF behavior of austenitic stainless steels. Indeed, our results have
384 shown that the SMAT allowed to increase the fatigue limit of samples loaded at $R_{TC} = -1$ by about +17 % for
385 both the 316L and 304L steels, while a reduction of -7 % was observed when samples were loaded at
386 $R_{TT} = +0.1$. For R_{TC} , such improvement has already been observed in fully reversed loading ($R = -1$), whether
387 the steel was loaded in tension-compression [32, 40] or alternating flexural or rotating bending [18, 40]. In
388 comparison, for R_{TT} , no direct comparison with data from the literature is available for stainless steels treated
389 by SMAT. While mechanical surface treatments are carried out to enhance the fatigue limit of materials, they
390 appear to potentially have the opposite effect and actually reduce it. In such case, it is most of the time attributed
391 to the modified surface roughness and generated surface defects. Thus, the first section of this discussion will
392 deal with the direct effect of the surface integrity on the fatigue behavior. This will be shown to be insufficient
393 to fully explain the differences in behavior. Then, the influence of the plastic deformation mechanisms on the
394 microstructure and hardness as well as the role of the residual stress evolutions and their effect on the fatigue
395 crack initiation mechanisms will be discussed.

396 4.1. Effect of the surface integrity on fatigue crack initiation

397 It is often proposed that the reduction in fatigue properties is due to surface defects that lead to faster
398 fatigue crack initiation and compensate the benefits of the surface compressive residual stresses and hardened
399 layer. This hypothesis can be found in several works focusing on a wide variety of materials and loading
400 conditions. Kumar et al. studied uniaxial tension-tension fatigue at $R = +0.1$ after 30 min and 60 min of SMAT
401 on the 718 Inconel superalloy [56] and on a Ti-6Al-4V titanium alloy [24]. While minimal effect was obtained
402 on the superalloy [56], the reduction of the fatigue limit observed after 60 min of SMAT in the Ti-alloy [24]
403 was proposed to be due to the increase of micro-damage linked to the increased treatment time. Tian et al. drew
404 a similar conclusion for a C-2000 nickel-based superalloy loaded at $R = +0.1$ under four-point bending for
405 which, after an improvement of 50 % in the fatigue limit after 30 min of SMAT, the fatigue life was
406 systematically reduced when the treatment duration was increased (60 min, 90 min and 180 min). This was
407 also discussed in the LCF and very high cycle fatigue (VHCF) regimes by Pandey et al. [57] and by
408 Gao et al. [58], who respectively studied a 7075 aluminium alloy and a TC11 titanium alloy loaded at $R = -1$
409 after different SMAT-processing times. For the Al-alloy, the number of cycles to failure was almost unchanged
410 after 30 sec and 60 sec of SMAT, increased for 180 sec but was reduced back to the initial performances after
411 300 sec of surface modification treatment [57]. The number of cycles to failure of the Ti-alloy was reduced by
412 approximately one to two decades for a “mild” surface modification condition and even further for a more
413 drastic SMAT one [58]. These negative behaviours were again attributed to the easier initiation of the fatigue
414 cracks which was cancelling the improved crack propagation resistance due to the compressive residual stress
415 layer [57, 58]. Maurel et al. studied the effect of SMAT duration when combined with ageing heat treatment
416 on the fatigue behavior of two aluminium alloys, namely a 2024 and 7075 series [26]. Some samples were aged
417 before SMAT and some after SMAT. By carrying SMAT on the soft solution treated condition (SMAT before
418 ageing), the fatigue limits were unchanged for the 2024 alloy and reduced by about 15 % for the 7075 one.
419 Comparatively, for both materials, conducting SMAT on the hardened material (SMAT after ageing) led to a
420 reduced samples surface roughness resulting in an increase of about 20 % of the fatigue limits.

421 Considering the non-negligible number of publications highlighting the fatigue life reduction after
422 severe SMAT-processing as the consequence of the increased roughness, it would be tempting to attribute the
423 reduction of the fatigue limit observed in this work at R_{TT} to the formation of dimples due to the high number
424 of impacts. However, as shown in Figure 2, such initiation mechanism on dimples was only detected for the
425 SMATed samples loaded at R_{TT} under low stress amplitudes. Instead, for the other R_{TT} conditions, crack
426 initiation mainly occurred around inclusions that were already present in the raw material while no obvious

427 difference was found in the initiation sites comparing polished and SMATed samples for the R_{TC} conditions.
428 However, it is clear that the “quality” of the surface has an effect on the fatigue properties. Indeed, for the
429 SMAT samples that were mirror polished and tested at R_{TT} , the properties were restored to those of the initially
430 polished material (Figure 1 b). Thus, the action of smoothing the surface after SMAT had a positive effect on
431 the fatigue properties. From this point of view, Bagherifard et al. also observed an additional (+10 %) increase
432 in the fatigue limit of severely shot peened low-alloy steel samples after conducting a grinding
433 post-processing [59]. An additional confirmation of the importance of the surface state in initiating the fracture
434 is the absence of any surface crack on the run-out samples (Figure 5). However, our overall results clearly
435 show that, even if the roughness of the surface and the presence of stress raisers must have an effect on the
436 fatigue properties, it is not the primary reason for the difference in behavior observed between the R_{TC} and R_{TT}
437 loading conditions.

438 4.2. Effects of the cyclic stress on the plastic deformation mechanisms

439 Exploring alternative hypotheses for the variable effectiveness of SMAT to enhance the fatigue limit
440 at R_{TC} and R_{TT} , the effect of the different type of loading has to be discussed. Indeed, the fact that half of the
441 fatigue life of the samples tested at R_{TC} occurs under a compressive state and that the maximum stress during
442 cycle is higher for R_{TT} imply very different macro- and micro- strains that may lead to the occurrence of
443 different damage mechanisms. The difference in material response to the different loading conditions can be
444 witnessed by two major observations. The first one is the self-heating of the samples observed at R_{TC} for a
445 10 Hz frequency but not at R_{TT} . The self-heating at R_{TC} is not detailed in the present paper but is completely
446 identical to the one observed on the 304L stainless steel studied in a previous work [40] in which the same
447 fatigue behavior at R_{TC} was obtained (Figure 1 a). In contrast, no self-heating was recorded at R_{TT} . To observe
448 such self-heating, a much higher loading frequency should probably be used. Indeed, Tian et al. also measured
449 a self-heating on a 316LN loaded at $R = -1$ at 10 Hz but had to increase the testing frequency to 70 Hz to start
450 observing relevant self-heating at $R = +0.1$ [60]. The second evidence is the difference in microstructure
451 evolution in the core of the sample between the R_{TC} and R_{TT} loading conditions. Indeed, during the tension-
452 compression cyclic loading of the SMATed samples, the martensitic transformation occurred at depth below
453 200 μm (Figure 6 a). Interestingly, this transformation did not occur in the regions closer to the surface at
454 100-200 μm , probably due to the too high density of dislocations already present in the SMATed highly
455 hardened domain that prevented the austenite to martensite phase transformation. This is in good accordance
456 with the literature about the conditions required for athermal martensitic transformation in steels. Indeed, it

457 was shown that enhancing the yield stress of the parent phase (austenite) by a moderate increase of the
458 dislocation density [61, 62] or decreasing the grain size [63] both lead to a reduction in the M_S temperature.
459 Such lowered value of M_S implies that a greater mechanical work is required to allow martensitic
460 transformation; in other words, a greater stability of the austenite in this region. In contrast, neither stress- nor
461 strain-assisted martensitic transformation was triggered under the tension-tension fatigue condition used in this
462 work. Due to the negative values of M_S and M_{d30} for this alloy (Table 1), a significant strain is required to
463 induce $\gamma \rightarrow \alpha'$ phase transformation, as it was the case in the first 100 μm due to the severe plastic deformation
464 induced by SMAT. The fact that phase transformation occurred during cyclic loading under R_{TC} and not under
465 R_{TT} conditions seems rather counter intuitive. Indeed, it is widely admitted that the martensite volume increases
466 with strain [61, 64] and such phenomena is considered in recent modelling [65]. Also, Lebedev et al. showed
467 that for a 18Cr-10Ni stainless steel, the martensitic transformation is more advanced when the sample is
468 subjected to tension than compression [66]. Then, considering that the samples are subjected to higher strains
469 for R_{TT} than R_{TC} and are exclusively undergoing tensile loading at R_{TT} , it would be fair to expect a higher
470 volume fraction of martensite for R_{TT} than R_{TC} . The exact opposite is observed here, indicating that other
471 parameters are affecting the stability of austenite when subjected to cyclic loading. Lebedev et al. also reported
472 that it is unusual to find martensite in fatigue loaded samples except on the crack path where the stress triaxiality
473 is much higher than in the rest of the samples [66] which might be an essential aspect to consider in order to
474 understand the observed phase transformation.

475 Nevertheless, even if these differences in the plastic deformation mechanisms and resulting
476 microstructures were observed due to the different loading conditions, they are not at the origin of the
477 differences in the fatigue properties. Indeed, the observed phase transformation is supposed to have negligible
478 influence on the surface fatigue crack initiation because it occurred 200 μm below the surface. In addition, in
479 Figure 1 the 304L and the 316L stainless steels were shown to have identical fatigue behavior at R_{TC} even if
480 Dureau et al. highlighted that the surface of the 304L was fully martensitic after SMAT [40]. Moreover, the
481 analysis of hardness gradient after different fatigue loading conditions revealed limited changes in the
482 hardening state in the SMAT affected region for R_{TC} and R_{TT} conditions. As the evolutions of hardness followed
483 the same trends, it should have an equally beneficial contribution to the fatigue life enhancement for both load
484 ratios after SMAT and, consequently, it is also not responsible for the fatigue life reduction at R_{TT} .

485 One of the major difference revealed by the analysis of the run-out samples is that the residual stress
486 gradient evolutions after fatigue were drastically different under R_{TC} and R_{TT} . The compressive stress state

487 relaxation observed for R_{TC} was commonly observed after fatigue loading for many materials and testing
488 conditions [4, 5, 19, 31, 40, 51] and sometimes even led to a fully relaxed stress field [34]. Comparatively, the
489 gradient reversion leading to the formation of tensile residual stress gradient generally occurs for quasi-static
490 loading or when overloads occur during fatigue [35, 67-71]. In our case, the inverted residual stress state was
491 formed after the first cycle of fatigue and remained during the whole fatigue life of the samples. As the internal
492 stresses redistributions are essentially a matter of mechanical equilibrium between the sub-surface layer
493 affected by the SMAT and the core, the maximum applied stress during cyclic loading governs the residual
494 stress evolutions. For the studied samples, the maximum applied loads during cycles were respectively
495 $\sigma_{R_{TC} \max}^{SMAT} = 240$ MPa and $\sigma_{R_{TT} \max}^{SMAT} = 477$ MPa. $\sigma_{R_{TC} \max}^{SMAT}$ is then equal to 35% of the maximum tensile stress
496 σ_{UTS} (= 650 MPa), and 110 % of the yield stress σ_{ys} (= 220 MPa). On the other hand, $\sigma_{R_{TT} \max}^{SMAT}$ is equal to 72%
497 of σ_{UTS} thus 215 % of σ_{ys} . As $\sigma_{R_{TC} \max}^{SMAT}$ was close to the yield stress, the core of the samples experienced small
498 strains at R_{TC} , leading to moderate residual stress relaxations. In contrast, $\sigma_{R_{TT} \max}^{SMAT}$ being twice the yield stress,
499 the applied tensile strain has reverted the distribution of residual stresses. In both cases, those redistributed and
500 stabilized residual stresses act as a local mean stress superimposed to the macroscopic loading, thus changing
501 the stress field during cycling. This can help to understand the differences in the observed fatigue crack
502 initiation mechanisms.

503 For the R_{TC} conditions, the maximum applied loads are just a few tens of MPa above the material
504 elastic limit, causing only moderate and localized plastic strain. As confirmed by the surface analysis in
505 Figure 2, these levels of plasticity are not large enough under the R_{TC} conditions to initiate cracking on
506 inclusions regardless of the stress amplitude, especially for the SMAT samples due to the surface compressive
507 residual stress. If Kakiuchi et al. observed one initiation on such calcium-aluminate inclusion in a 304L
508 stainless steel treated by SMAT and then loaded at $R = -1$ under rotating bending [72], it should be noticed that
509 their fatigue tests were conducted at a temperature of 300 °C. It is possible that this elevated temperature can
510 facilitate the use of these particles as stress raisers because it enhances the differences in mechanical properties
511 between the austenitic matrix and the hard inclusion.

512 For the R_{TT} conditions, the much higher applied stress than for R_{TC} led to macroscopic straining of the
513 samples highlighted by the high density of slip bands in Figure 2, thus damaging the inclusions interface with
514 the steel matrix. This allowed the inclusions to be activated as initiation sites. This is particularly true for the

515 SMATed and SMAT + polished samples due to the superimposed macroscopic tensile loading and surface high
516 tensile residual stress states.

517 Finally, as the surface inspection of the run-out samples never revealed non-propagating fatigue
518 cracks, the resistance of the material to fatigue crack initiation was shown to rule the fatigue limit in the high
519 cycle fatigue regime. Then, the redistributed residual stress fields were taken into account into a Crossland
520 fatigue initiation criterion and provided a good description of both the effect of load ratio and SMAT. The
521 residual stress state was then considered the first-order parameter governing the fatigue performance of
522 SMATed austenitic stainless steels samples. Therefore, the development of numerical models to predict the
523 cyclic response of SMATed samples and the residual stress field evolutions after such cyclic loading seems to
524 be a very interesting way of predicting the fatigue life of gradient microstructure stainless steels components
525 under various loading conditions.

526 **6. Conclusions**

527 Uniaxial fatigue tests have been conducted on an austenitic stainless steel with load ratios $R_{TC} = -1$ and
528 $R_{TT} = +0.1$, to evaluate the high cycle fatigue performance of the gradient microstructure generated by SMAT
529 in a context of local or general plasticity. The fatigue limit change resulting from SMAT was beneficial
530 at $R_{TC} = -1$ (+17 %) and detrimental at $R_{TT} = +0.1$ (-7 %).

531 After fatigue loading, no cracks were detected at the surface of any of the run-out samples, indicating that the
532 resistance to fatigue crack initiation was governing the fatigue limit in the HCF regime. Processing inclusions
533 already present in the initial material were the predominant initiation sites for crack nucleation for R_{TT} rather
534 than surface defects. The evolution of residual stresses was proved to be the primary parameter governing the
535 fatigue response: the compressive residual stress generated by SMAT was partially relaxed at R_{TC} while it was
536 fully reverted after only one cycle of R_{TT} loading.

537 The beneficial effect on the fatigue limit (improved by +17 %) for $R_{TC} = -1$ loading is due to the sub-surface
538 compressive residual stresses present in the hardened gradient microstructure that overcome the negative effect
539 of the surface defects induced by SMAT. During fatigue loading at R_{TC} , self-heating of all the specimens
540 occurred together with sub-surface martensitic transformation for the SMATed samples. Nevertheless, these
541 two modifications had a negligible impact on the fatigue properties.

542 The detrimental effect on the fatigue limit (reduced by -7 %) for $R_{TT} = +0.1$ is associated to the high imposed
543 macroscopic stresses that caused a complete reversion of the compressive residual stress gradient towards
544 tension. This very high tensile stress leads to faster fatigue crack initiation compared to the untreated material.
545 In this case, no self-heating nor sub-surface martensitic transformation were revealed, but the much higher
546 stress at R_{TT} was proposed to be responsible for the initiations on inclusions. In this case, the combined negative
547 effects of tensile residual stresses and surface roughness leads to a slightly reduced fatigue limit for SMAT
548 specimens.

549 For the R_{TT} loading condition, a mirror polishing procedure after SMAT allowed to restore the fatigue limit
550 (same as the untreated condition) but did not improve it. This is a confirmation that (i) the redistribution of
551 residual stress was of primary importance for controlling the high cycle fatigue behavior and (ii) the surface
552 defects created by SMAT were not responsible for the incapacity of the SMAT to improve the fatigue limit at
553 R_{TT} .

554

555 **Acknowledgement**

556 This work was supported by the French State through the program “Investment in the future” operated by the
557 National Research Agency (ANR), referenced by ANR-11-LABX-0008-01 (Labex DAMAS).

558 This work was also supported by the CPER FEDER project of Région Nouvelle Aquitaine.

559 **Declaration of competing interest**

560 The authors declare that they have no known competing financial interests or personal relationships that could
561 have appeared to influence the work reported in this paper.

562 **References**

563 [1] Y. Miyamoto, W.A. Kaysser, B.H. Rabin, A. Kawasaki, R.G. Ford, Functionally Graded Materials:
564 Design, Processing and Applications, Kluwer Academic Publishers, Hingham, MA (US), United States,
565 (1999). <https://doi.org/10.1007/978-1-4615-5301-4>

566 [2] B. Kieback, A. Neubrand, H. Riedel, Processing techniques for functionally graded materials,
567 Materials Science and Engineering: A, 362(1-2) (2003) 81-106. DOI: [https://doi.org/10.1016/S0921-](https://doi.org/10.1016/S0921-5093(03)00578-1)
568 5093(03)00578-1

- 569 [3] K. Dalaei, B. Karlsson, Influence of shot peening on fatigue durability of normalized steel subjected
570 to variable amplitude loading, *International journal of fatigue*, 38 (2012) 75-83.
571 DOI: <https://doi.org/10.1016/j.ijfatigue.2011.11.011>
- 572 [4] J.C. Kim, S.K. Cheong, H. Noguchi, Residual stress relaxation and low-and high-cycle fatigue
573 behavior of shot-peened medium-carbon steel, *International Journal of Fatigue*, 56 (2013) 114-122.
574 DOI: <https://doi.org/10.1016/j.ijfatigue.2013.07.001>
- 575 [5] M. Benedetti, V. Fontanari, C. Santus, M. Bandini, Notch fatigue behavior of shot peened high-
576 strength aluminium alloys: Experiments and predictions using a critical distance method, *International Journal*
577 *of Fatigue*, 32(10) (2010) 1600-1611. DOI: <https://doi.org/10.1016/j.ijfatigue.2010.02.012>
- 578 [6] H. Luong, M.R. Hill, The effects of laser peening and shot peening on high cycle fatigue in 7050-
579 T7451 aluminum alloy, *Materials Science and Engineering: A*, 527(3) (2010) 699-707.
580 DOI: <https://doi.org/10.1016/j.msea.2009.08.045>
- 581 [7] M. Benedetti, T. Bortolamedi, V. Fontanari, F. Frenzo, Bending fatigue behavior of differently shot
582 peened Al 6082 T5 alloy, *International journal of fatigue*, 26(8) (2004) 889-897.
583 DOI: <https://doi.org/10.1016/j.ijfatigue.2003.12.003>
- 584 [8] S. Bagheri, M. Guagliano, Review of shot peening processes to obtain nanocrystalline surfaces in
585 metal alloys, *Surface Engineering*, 25(1) (2009) 3-14. DOI: <https://doi.org/10.1179/026708408X334087>
- 586 [9] J. Azadmanjiri, C.C. Berndt, A. Kapoor, C. Wen, Development of surface nano-crystallization in
587 alloys by surface mechanical attrition treatment (SMAT), *Critical Reviews in Solid State and Materials*
588 *Sciences*, 40(3) (2015) 164-181. DOI: <https://doi.org/10.1080/10408436.2014.978446>
- 589 [10] T. Grosdidier, M. Novelli, Recent developments in the application of surface mechanical attrition
590 treatments for improved gradient structures: processing parameters and surface reactivity. *Materials*
591 *transactions*, 60(7) (2019) 1344-1355. DOI: <https://doi.org/10.2320/matertrans.MF201929>
- 592 [11] D. Kumar, S. Idapalapati, W. Wang, S. Narasimalu, Effect of surface mechanical treatments on the
593 microstructure-property-performance of engineering alloys, *Materials*, 12(16) (2019) 2503.
594 DOI: <https://doi.org/10.3390/ma12162503>

- 595 [12] T.O. Olugbade, J. Lu, Literature review on the mechanical properties of materials after surface
596 mechanical attrition treatment (SMAT), *Nano Materials Science*, 2(1) (2020) 3-31.
597 DOI: <https://doi.org/10.1016/j.nanoms.2020.04.002>
- 598 [13] Y. Samih, B. Beausir, B. Bolle, T. Grosdidier, In-depth quantitative analysis of the microstructures
599 produced by Surface Mechanical Attrition Treatment (SMAT), *Materials characterization*, 83 (2013) 129-138.
600 DOI: <https://doi.org/10.1016/j.matchar.2013.06.006>
- 601 [14] G. Proust, D. Retraint, M. Chemkhi, A. Roos, C. Demangel, Electron backscatter diffraction and
602 transmission Kikuchi diffraction analysis of an austenitic stainless steel subjected to surface mechanical
603 attrition treatment and plasma nitriding, *Microscopy and Microanalysis*, 21(4) (2015) 919-926.
604 DOI: <https://doi.org/10.1017/S1431927615000793>
- 605 [15] C. Xin, D. Yang, Q. Sun, L. Xiao, J. Sun, Thermal stability of nanogradient microstructure produced
606 by surface mechanical rolling treatment in Zircaloy-4, *Journal of Materials Science*, 55(11) (2020) 4926-4939.
607 DOI: <https://doi.org/10.1007/s10853-019-04303-z>
- 608 [16] K. Skowron, E. Dryzek, M. Wróbel, P. Nowak, M. Marciszko-Wiąckowska, L. Le Joncour, M.
609 François, B. Panicaud, A. Baczmański, Gradient Microstructure Induced by Surface Mechanical Attrition
610 Treatment (SMAT) in Magnesium Studied Using Positron Annihilation Spectroscopy and Complementary
611 Methods, *Materials*, 13(18) (2020) 4002. DOI: <https://doi.org/10.3390/ma13184002>
- 612 [17] J.C. Villegas, L.L. Shaw, K. Dai, W. Yuan, J. Tian, P.K. Liaw, D.L. Klarstrom, Enhanced fatigue
613 resistance of a nickel-based hastelloy induced by a surface nanocrystallization and hardening process,
614 *Philosophical magazine letters*, 85(8) (2005) 427-438. DOI: <https://doi.org/10.1080/09500830500311705>
- 615 [18] J. Uusitalo, L.P. Karjalainen, D. Retraint, M. Palosaari, Fatigue properties of steels with ultrasonic
616 attrition treated surface layers, In: *Materials science forum*, Trans Tech Publications Ltd., Vol. 604 (2009)
617 239-248. DOI: <https://doi.org/10.4028/www.scientific.net/MSF.604-605.239>
- 618 [19] L.L. Shaw, J.W. Tian, A.L. Ortiz, K. Dai, J.C. Villegas, P.K. Liaw, R. Ren, D.L. Klarstrom, A direct
619 comparison in the fatigue resistance enhanced by surface severe plastic deformation and shot peening in a C-
620 2000 superalloy, *Materials Science and Engineering: A*, 527(4-5) (2010) 986-994.
621 DOI: <https://doi.org/10.1016/j.msea.2009.10.028>

- 622 [20] L. Yang, N.R. Tao, K. Lu, L. Lu, Enhanced fatigue resistance of Cu with a gradient nanograined
623 surface layer, *Scripta Materialia*, 68(10) (2013) 801-804.
624 DOI: <https://doi.org/10.1016/j.scriptamat.2013.01.031>
- 625 [21] M.K. Khan, M.E. Fitzpatrick, Q.Y. Wang, Y.S. Pyoun, A. Amanov, Effect of ultrasonic nanocrystal
626 surface modification on residual stress and fatigue cracking in engineering alloys, *Fatigue & Fracture of
627 Engineering Materials & Structures*, 41(4) (2018) 844-855. DOI: <https://doi.org/10.1111/ffe.12732>
- 628 [22] S. Bagherifard, I. Fernandez-Pariente, R. Ghelichi, M. Guagliano, Effect of severe shot peening on
629 microstructure and fatigue strength of cast iron, *International Journal of Fatigue*, 65 (2014) 64-70.
630 DOI: <https://doi.org/10.1016/j.ijfatigue.2013.08.022>
- 631 [23] J.W. Tian, J.C. Villegas, W. Yuan, D. Fielden, L. Shaw, P.K. Liaw, D.L. Klarstrom, A study of the
632 effect of nanostructured surface layers on the fatigue behaviors of a C-2000 superalloy, *Materials Science and
633 Engineering: A*, 468 (2007) 164-170. DOI: <https://doi.org/10.1016/j.msea.2006.10.150>
- 634 [24] S.A. Kumar, S.G.S. Raman, T.S. Narayanan, Influence of surface mechanical attrition treatment
635 duration on fatigue lives of Ti-6Al-4V, *Transactions of the Indian Institute of Metals*, 67(1) (2014) 137-141.
636 DOI: <https://doi.org/10.1007/s12666-013-0322-2>
- 637 [25] Y. Feng, S. Hu, D. Wang, L. Cui, Formation of short crack and its effect on fatigue properties of
638 ultrasonic peening treatment S355 steel, *Materials & Design*, 89 (2016) 507-515.
639 DOI: <https://doi.org/10.1016/j.matdes.2015.10.009>
- 640 [26] P. Maurel, L. Weiss, T. Grosdidier, P. Bocher, How does surface integrity of nanostructured surfaces
641 induced by severe plastic deformation influence fatigue behaviors of Al alloys with enhanced
642 precipitation?, *International Journal of Fatigue*, 140 (2020) 105792.
643 DOI: <https://doi.org/10.1016/j.ijfatigue.2020.105792>
- 644 [27] P. Maurel, L. Weiss, P. Bocher, T. Grosdidier, Effects of SMAT at cryogenic and room temperatures
645 on the kink band and martensite formations with associated fatigue resistance in a β -metastable titanium
646 alloy, *Materials Science and Engineering: A*, 803 (2021) 140618.
647 DOI: <https://doi.org/10.1016/j.msea.2020.140618>

- 648 [28] F.K. Yan, G.Z. Liu, N.R. Tao, K. Lu, Strength and ductility of 316L austenitic stainless steel
649 strengthened by nano-scale twin bundles, *Acta Materialia*, 60(3) (2012) 1059-1071.
650 DOI: <https://doi.org/10.1016/j.actamat.2011.11.009>
- 651 [29] J. Li, Y. Cao, B. Gao, Y. Li, Y. Zhu, Superior strength and ductility of 316L stainless steel with
652 heterogeneous lamella structure, *Journal of Materials Science*, 53(14) (2018) 10442-10456.
653 DOI: <https://doi.org/10.1007/s10853-018-2322-4>
- 654 [30] H. Ueno, K. Kakihata, Y. Kaneko, S. Hashimoto, A. Vinogradov, Enhanced fatigue properties of
655 nanostructured austenitic SUS 316L stainless steel, *Acta Materialia*, 59(18) (2011) 7060-7069.
656 DOI: <https://doi.org/10.1016/j.actamat.2011.07.061>
- 657 [31] K. Masaki, Y. Ochi, T. Matsumura, Initiation and propagation behavior of fatigue cracks in hard-shot
658 peened Type 316L steel in high cycle fatigue, *Fatigue & Fracture of Engineering Materials & Structures*, 27(12)
659 (2004) 1137-1145. DOI: <https://doi.org/10.1111/j.1460-2695.2004.00824.x>
- 660 [32] T. Roland, D. Reirant, K. Lu, J. Lu, Fatigue life improvement through surface nanostructuring of
661 stainless steel by means of surface mechanical attrition treatment, *Scripta Materialia*, 54(11) (2006) 1949-1954.
662 DOI: <https://doi.org/10.1016/j.scriptamat.2006.01.049>
- 663 [33] Z. Sun, M. Chemkhi, P. Kanoute, D. Reirant, Fatigue properties of a biomedical 316L steel processed
664 by surface mechanical attrition, In: *IOP Conference Series: Materials Science and Engineering*, 63 (2014)
665 012021. DOI: <https://doi.org/10.1088/1757-899x/63/1/012021>
- 666 [34] Z. Sun, J. Zhou, D. Reirant, T. Baudin, A.L. Helbert, F. Brisset, P. Kanouté, Low cycle fatigue of
667 316L stainless steel processed by surface mechanical attrition treatment (SMAT), In: *MATEC Web of
668 Conferences*, EDP Sciences, 165 (2018) 15002. DOI: <https://doi.org/10.1051/mateconf/201816515002>
- 669 [35] H.W. Huang, Z.B. Wang, J. Lu, K. Lu, Fatigue behaviors of AISI 316L stainless steel with a gradient
670 nanostructured surface layer, *Acta Materialia*, 87 (2015) 150-160.
671 DOI: <https://doi.org/10.1016/j.actamat.2014.12.057>
- 672 [36] SONATS company website available online: <https://sonats-et.com/> (accessed on 27 October 2021).
- 673 [37] B. Beausir, J.-J. Fundenberger, Analysis Tools for Electron and X-ray diffraction, ATEX - software,
674 www.atex-software.eu, Université de Lorraine - Metz, (2017).

- 675 [38] M. G. Moore, W. P. Evans, Mathematical correction for stress in removed layers in X-ray diffraction
676 residual stress analysis. SAE transactions, (1958) 340-345. DOI: <https://doi.org/10.4271/580035>
- 677 [39] C.E. Stromeyer, The determination of fatigue limits under alternating stress conditions. Proceedings
678 of the Royal Society of London, Series A, Containing Papers of a Mathematical and Physical Character,
679 90(620) (1914) 411-425. DOI: <https://doi.org/10.1098/rspa.1914.0066>
- 680 [40] C. Dureau, M. Novelli, M. Arzaghi, R. Massion, P. Bocher, Y. Nadot, T. Grosdidier, On the influence
681 of ultrasonic surface mechanical attrition treatment (SMAT) on the fatigue behavior of the 304L austenitic
682 stainless steel, *Metals*, 10(1) (2020) 100. DOI: <https://doi.org/10.3390/met10010100>
- 683 [41] L. Zhang, B.G. Thomas, Inclusions in continuous casting of steel, In: XXIV National Steelmaking
684 Symposium, Morelia, Mexico, 26 (2003) 28.
- 685 [42] Y. Samih, M. Novelli, T. Thiriet, B. Bolle, N. Allain, J.-J. Funderberger, G. Marcos, T. Czerwicz, T.
686 Grosdidier, Plastic deformation to enhance plasma-assisted nitriding: On surface contamination induced by
687 Surface Mechanical Attrition Treatment, In: IOP Conference Series: Materials Science and Engineering, 63
688 (2014) 012020. DOI: <https://doi.org/10.1088/1757-899x/63/1/012020>
- 689 [43] M. Chemkhi, D. Reirant, A. Roos, C. Demangel, Role and effect of mechanical polishing on the
690 enhancement of the duplex mechanical attrition/plasma nitriding treatment of AISI 316L steel, *Surface and*
691 *Coatings Technology*, 325 (2017) 454-461. DOI: <https://doi.org/10.1016/j.surfcoat.2017.06.052>
- 692 [44] P. Maurel, L. Weiss, P. Bocher, E. Fleury, T. Grosdidier, Oxide dependent wear mechanisms of
693 titanium against a steel counterface: Influence of SMAT nanostructured surface, *Wear*, 430 (2019) 245-255.
694 DOI: <https://doi.org/10.1016/j.wear.2019.05.007>
- 695 [45] T. Niendorf, F. Rubitschek, H.J. Maier, D. Canadinc, I. Karaman, On the fatigue crack growth–
696 microstructure relationship in ultrafine-grained interstitial-free steel, *Journal of materials science*, 45(17)
697 (2010) 4813-4821. DOI: <https://doi.org/10.1007/s10853-010-4511-7>
- 698 [46] K. Hockauf, M. Hockauf, M.X. Wagner, T. Lampke, T. Halle, Fatigue crack propagation in an ECAP-
699 processed aluminium alloy–influence of shear plane orientation, *Materialwissenschaft und*
700 *Werkstofftechnik*, 43(7) (2012) 609-616. DOI: <http://dx.doi.org/10.1002/mawe.201200008>

701 [47] M. Arzaghi, C. Sarrazin-Baudoux, J. Petit, Fatigue crack growth in ultrafine-grained copper obtained
702 by ECAP, In: *Advanced Materials Research*, Trans Tech Publications Ltd., 891 (2014) 1099-1104.
703 DOI: <https://doi.org/10.4028/www.scientific.net/AMR.891-892.1099>

704 [48] R. Blonde, H.L. Chan, N. Allain-Bonasso, B. Bolle, T. Grosdidier, J. Lu, Evolution of texture and
705 microstructure in pulsed electro-deposited Cu treated by Surface Mechanical Attrition Treatment
706 (SMAT), *Journal of Alloys and Compounds*, 504 (2010) S410-S413.
707 DOI: <https://doi.org/10.1016/j.jallcom.2010.04.040>

708 [49] B. Cotterell, J. Rice, Slightly curved or kinked cracks, *International journal of fracture*, 16(2) (1980)
709 155-169. DOI: <https://doi.org/10.1007/BF00012619>

710 [50] M. Novelli, P. Bocher, T. Grosdidier, Effect of cryogenic temperatures and processing parameters on
711 gradient-structure of a stainless steel treated by ultrasonic surface mechanical attrition treatment, *Materials*
712 *Characterization*, 139 (2018) 197-207. DOI: <https://doi.org/10.1016/j.matchar.2018.02.028>

713 [51] Y.B. Lei, Z.B. Wang, J.L. Xu, K. Lu, Simultaneous enhancement of stress-and strain-controlled
714 fatigue properties in 316L stainless steel with gradient nanostructure, *Acta Materialia*, 168 (2019) 133-142.
715 DOI: <https://doi.org/10.1016/j.actamat.2019.02.008>

716 [52] F. Yin, S. Hu, R. Xu, X. Han, D. Qian, W. Wei, L. Hua, K. Zhao, Strain rate sensitivity of the
717 ultrastrong gradient nanocrystalline 316L stainless steel and its rate-dependent modeling at
718 nanoscale, *International Journal of Plasticity*, 129 (2020) 102696.
719 DOI: <https://doi.org/10.1016/j.ijplas.2020.102696>

720 [53] M. Novelli, J.-J. Fundenberger, P. Bocher, T. Grosdidier, On the effectiveness of surface severe plastic
721 deformation by shot peening at cryogenic temperature, *Applied Surface Science*, 389 (2016) 1169-1174.
722 DOI: <https://doi.org/10.1016/j.apsusc.2016.08.009>

723 [54] B. Crossland, Effect of large hydrostatic pressures on the torsional fatigue strength of an alloy steel,
724 In: *Proceedings of the International Conference on Fatigue of Metals*, Institution of Mechanical Engineers
725 London, 138 (1956) 12-12.

726 [55] P. Mu, Y. Nadot, C. Nadot-Martin, A. Chabod, I. Serrano-Munoz, C. Verdu, Influence of casting
727 defects on the fatigue behavior of cast aluminum AS7G06-T6, *International Journal of Fatigue*, 63 (2014) 97-
728 109. DOI: <https://doi.org/10.1016/j.ijfatigue.2014.01.011>

- 729 [56] S.A. Kumar, S.G.S. Raman, T.S. Narayanan, Effect of surface mechanical attrition treatment on
730 fatigue lives of alloy 718, *Transactions of the Indian Institute of Metals*, 65(5) (2012) 473-477.
731 DOI: <https://doi.org/10.1007/s12666-012-0154-5>
- 732 [57] V. Pandey, K. Chattopadhyay, N.S. Srinivas, V. Singh, Role of ultrasonic shot peening on low cycle
733 fatigue behavior of 7075 aluminium alloy, *International Journal of Fatigue*, 103 (2017) 426-435.
734 DOI: <https://doi.org/10.1016/j.ijfatigue.2017.06.033>
- 735 [58] T. Gao, Z. Sun, H. Xue, D. Reirant, Effect of Surface Mechanical Attrition Treatment on the very
736 high cycle fatigue behavior of TC11, In: *MATEC Web of Conferences*, EDP Sciences, 165 (2018) 09001.
737 DOI: <https://doi.org/10.1051/matecconf/201816509001>
- 738 [59] S. Bagherifard, M. Guagliano, Fatigue behavior of a low-alloy steel with nanostructured surface
739 obtained by severe shot peening, *Engineering Fracture Mechanics*, 81 (2012) 56-68.
740 DOI: <https://doi.org/10.1016/j.engfracmech.2011.06.011>
- 741 [60] H. Tian, P.K. Liaw, D.E. Fielden, C.R. Brooks, M.D. Brotherton, L. Jiang, B. Yang, H. Wang, J.P.
742 Strizak, L.K. Mansur, Effects of frequency on fatigue behavior of type 316 low-carbon, nitrogen-added
743 stainless steel in air and mercury for the spallation neutron source, *Metallurgical and materials transactions A*,
744 37(1) (2006) 163-173. DOI: <https://doi.org/10.1007/s11661-006-0161-4>
- 745 [61] G.B. Olson, M. Cohen, Kinetics of strain-induced martensitic nucleation, *Metallurgical transactions*
746 *A*, 6(4) (1975) 791. DOI: <https://doi.org/10.1007/BF02672301>
- 747 [62] M. Tokizane, The effect of tensile pre-straining on nucleation of martensite in an Fe-Ni-C
748 alloy, *Scripta Metallurgica*, 10(5) (1976) 459-462. DOI: [https://doi.org/10.1016/0036-9748\(76\)90173-3](https://doi.org/10.1016/0036-9748(76)90173-3)
- 749 [63] S. Kajiwara, Roles of dislocations and grain boundaries in martensite nucleation, *Metallurgical and*
750 *Materials Transactions A*, 17(10) (1986) 1693-1702. DOI: <https://doi.org/10.1007/BF02817268>
- 751 [64] D. Hennessy, G. Steckel, C. Altstetter, Phase transformation of stainless steel during
752 fatigue, *Metallurgical Transactions A*, 7(3) (1976) 415-424. DOI: <https://doi.org/10.1007/BF02642838>
- 753 [65] E.I. Galindo-Nava, P.E.J. Rivera-Díaz-del-Castillo, Understanding martensite and twin formation in
754 austenitic steels: A model describing TRIP and TWIP effects, *Acta Materialia*, 128 (2017) 120-134.
755 DOI: <https://doi.org/10.1016/j.actamat.2017.02.004>

- 756 [66] A.A. Lebedev, V.V. Kosarchuk, Influence of phase transformations on the mechanical properties of
757 austenitic stainless steels, *International Journal of Plasticity*, 16(7-8) (2000) 749-767.
758 DOI: [https://doi.org/10.1016/S0749-6419\(99\)00085-6](https://doi.org/10.1016/S0749-6419(99)00085-6)
- 759 [67] A. Wick, V. Schulze, O. Vöhringer, Effects of warm peening on fatigue life and relaxation behavior
760 of residual stresses in AISI 4140 steel, *Materials Science and Engineering: A*, 293(1-2) (2000) 191-197.
761 DOI: [https://doi.org/10.1016/S0921-5093\(00\)01035-2](https://doi.org/10.1016/S0921-5093(00)01035-2)
- 762 [68] K. Dalaei, B. Karlsson, L.E. Svensson, Stability of shot peening induced residual stresses and their
763 influence on fatigue lifetime, *Materials Science and Engineering: A*, 528(3) (2011) 1008-1015.
764 DOI: <https://doi.org/10.1016/j.msea.2010.09.050>
- 765 [69] W.Z. Zhuang, G.R. Halford Investigation of residual stress relaxation under cyclic load, *International*
766 *journal of fatigue*, 23 (2001) 31-37. DOI: [https://doi.org/10.1016/S0142-1123\(01\)00132-3](https://doi.org/10.1016/S0142-1123(01)00132-3)
- 767 [70] K. Dalaei, B. Karlsson, Influence of overloading on fatigue durability and stability of residual stresses
768 in shot peened normalized steel, *Materials Science and Engineering: A*, 528(24) (2011) 7323-7330.
769 DOI: <https://doi.org/10.1016/j.msea.2011.06.002>
- 770 [71] D.J. Buchanan, R. John, Residual stress redistribution in shot peened samples subject to mechanical
771 loading, *Materials Science and Engineering: A*, 615 (2014) 70-78.
772 DOI: <https://doi.org/10.1016/j.msea.2014.06.118>
- 773 [72] T. Kakiuchi, Y. Uematsu, N. Hasegawa, E. Kondoh, Effect of ultrasonic shot peening on high cycle
774 fatigue behavior in type 304 stainless steel at elevated temperature, *J. Soc. Mater. Sci.* 65 (2016) 325–330.
775 DOI: <https://doi.org/10.2472/jsms.65.325>

776

Table 1 Chemical composition of the studied 316L stainless steel

	C	Mn	Si	S	P	Cr	Ni	Mo	Cu	N	Fe	M_S [° C]	M_{d30} [° C]
Wt [%]	0.029	1.499	0.341	0.03	0.22	16.605	10.370	2.036	0.127	0.047	Balance	-210	-1

777

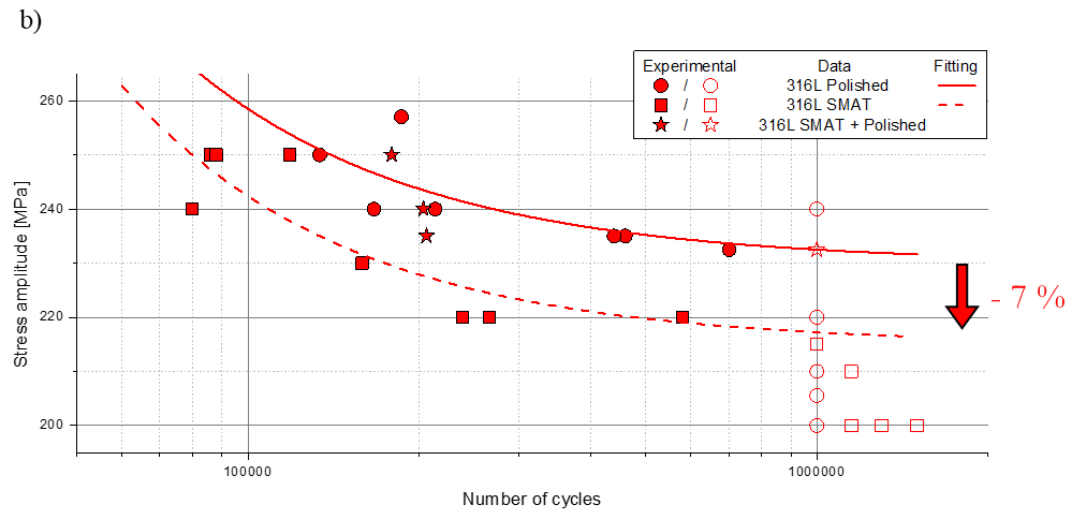
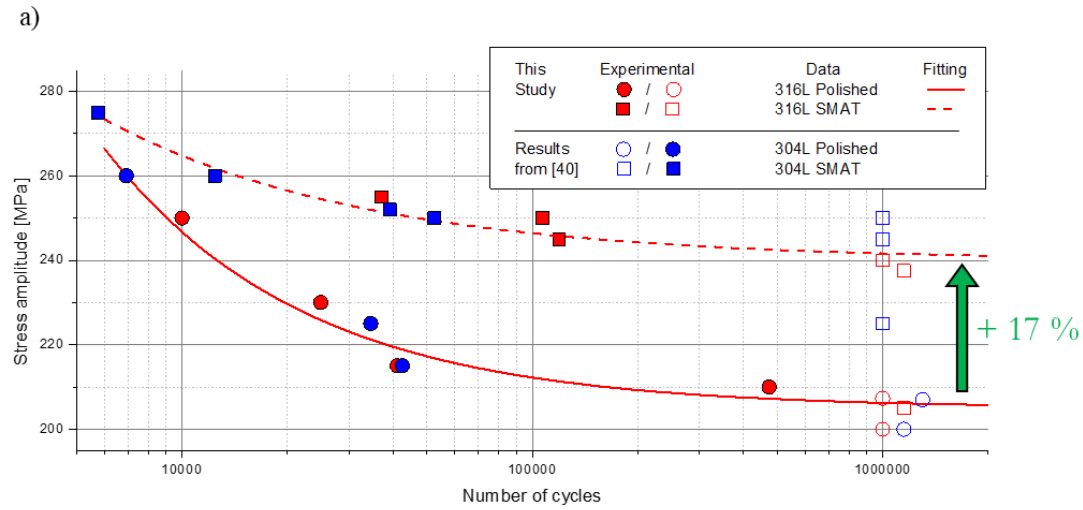
Table 2 Different a) fatigue testing conditions and b) analysed unbroken samples

a)

Testing condition name	Step 1	Step 2	Step 3	Step 4	Step 5	Ra [μm]
Initially polished	Heat treated 900 °C 40 min	Machined	Mirror polished	/	/	$0.017 \pm 2.5 \cdot 10^{-3}$
SMAT				SMATed	/	1.621 ± 0.23
SMAT + polished					Mirror polished	$0.018 \pm 1.4 \cdot 10^{-3}$

b)

Analysed unbroken sample	Load ratio	Stress amplitude [MPa]	Number of cycles
SMAT	/	/	/
SMAT + Fat R_{TC}	-1	240	$2 \cdot 10^6$
SMAT + Fat R_{TT}	+0.1	215	$4 \cdot 10^6$
SMAT + 1Cy R_{TT}	+0.1	215	1



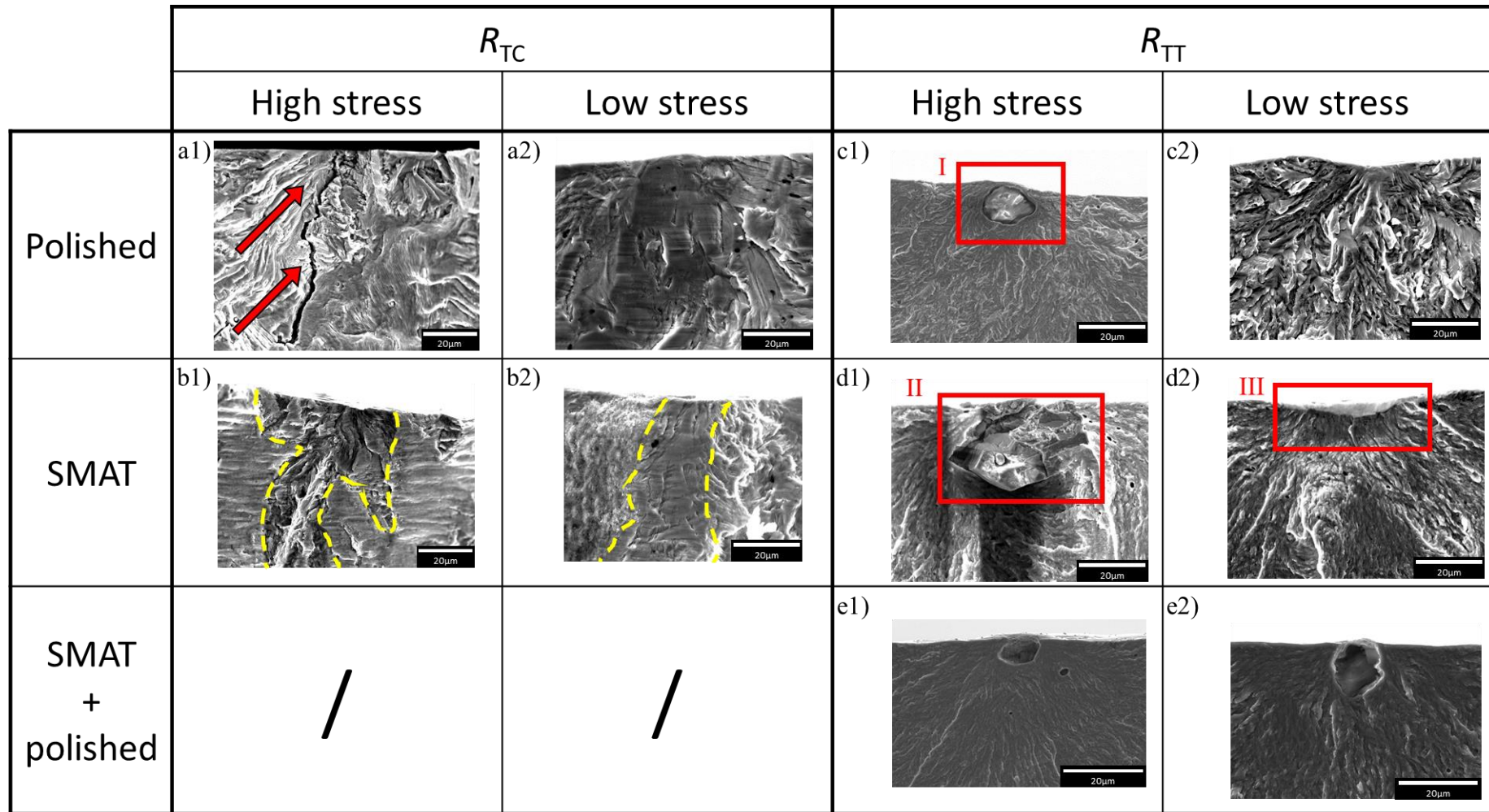
779

780

Figure 1 Wöhler curves of a) polished and SMAT 316L and 304L samples loaded at $R_{TC}=-1$ and b) polished, SMAT and SMAT + polished 316L samples loaded at

781

$R_{TT}=+0.1$



782

783

784

Figure 2 SEM images of the characteristic initiation sites for a) R_{TC} polished, b) R_{TC} SMAT, c) R_{TT} polished, d) R_{TT} SMAT and e) R_{TT} SMAT + polished samples for respectively 1) high and 2) low stress amplitudes

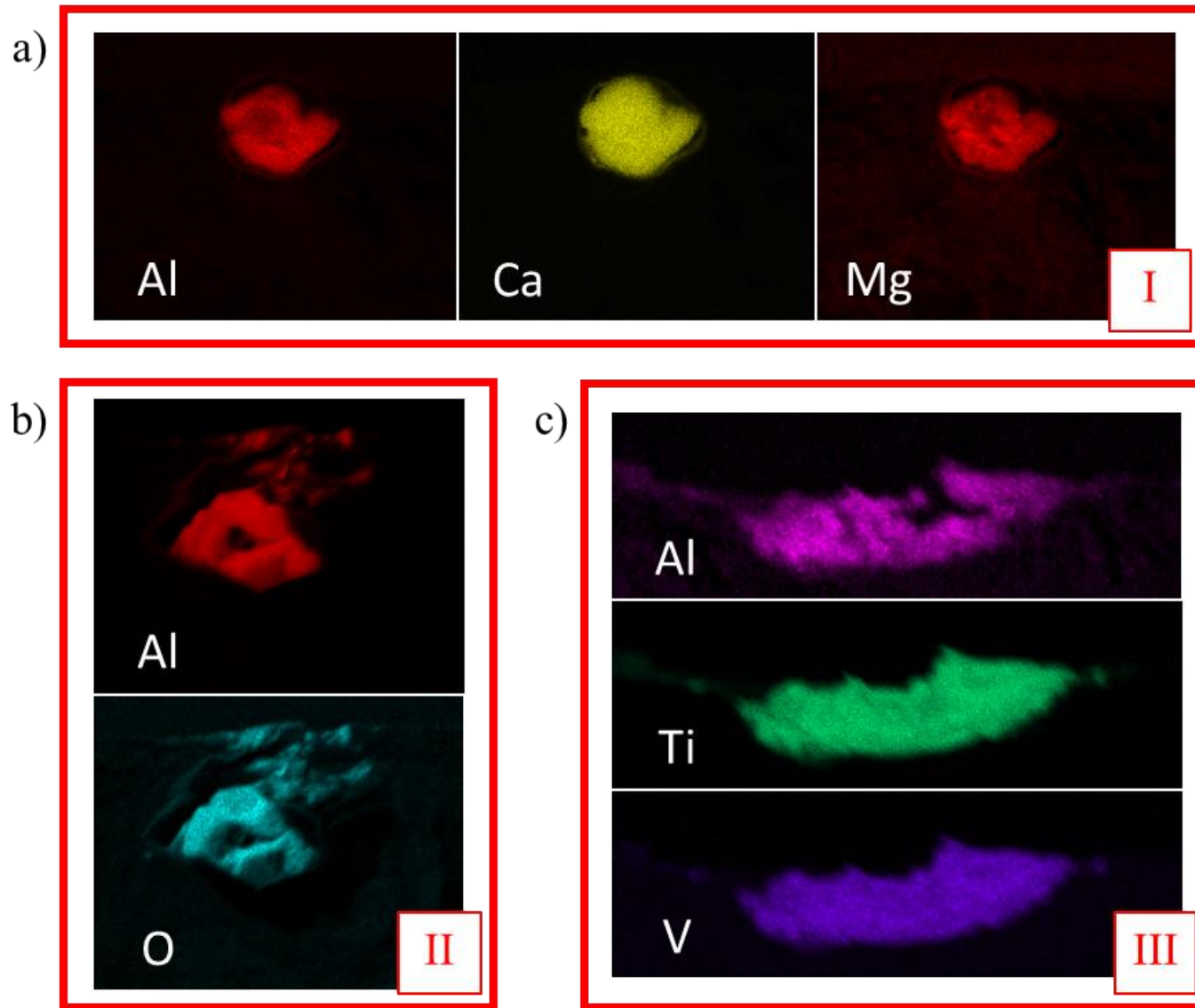
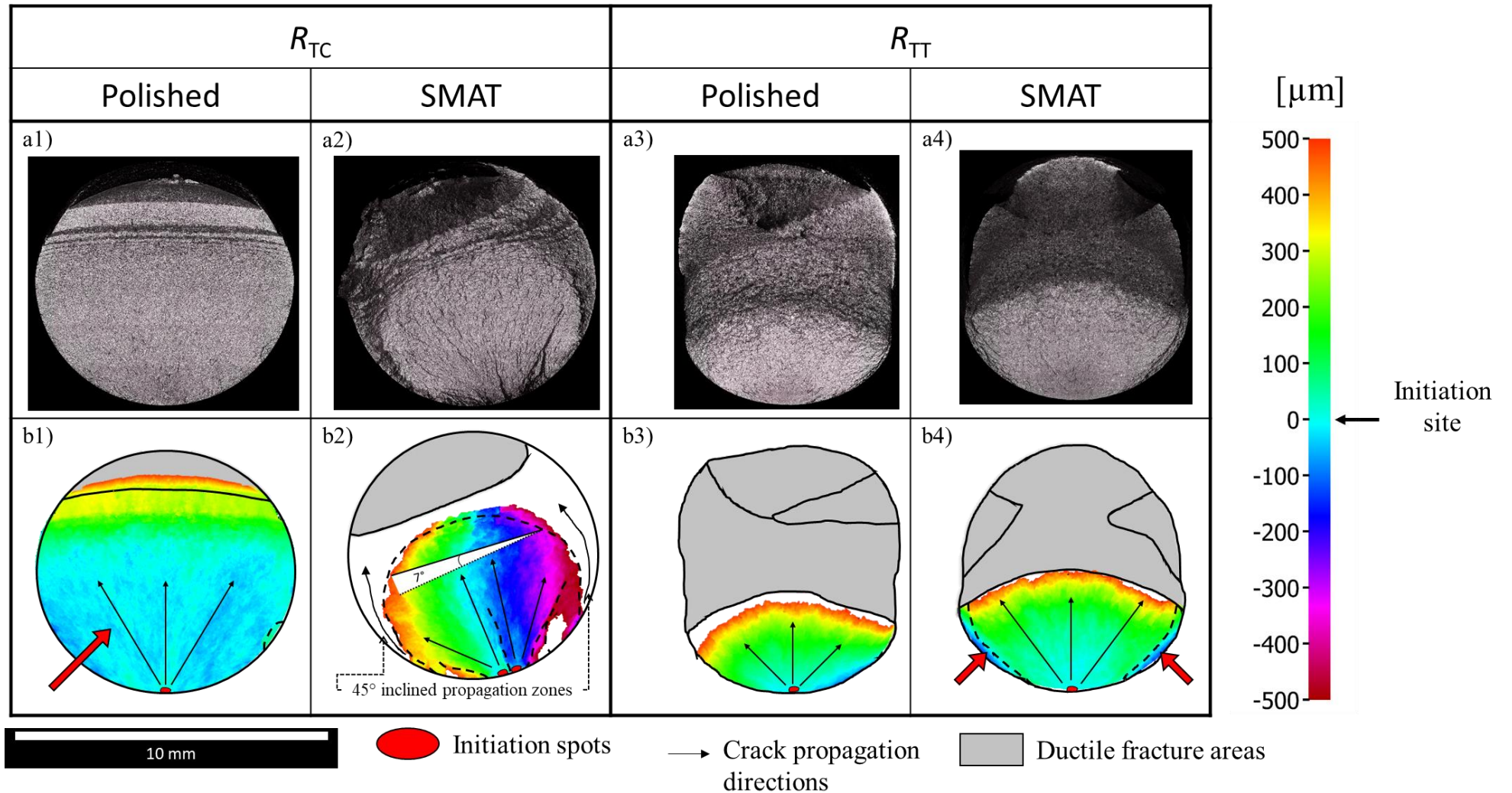


Figure 3 EDX maps corresponding to the regions highlighted in red in Figure 2

785

786



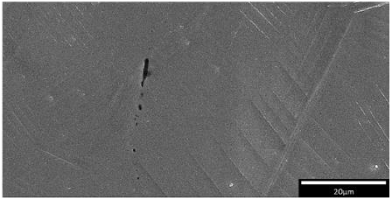
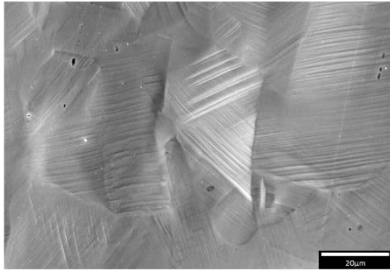
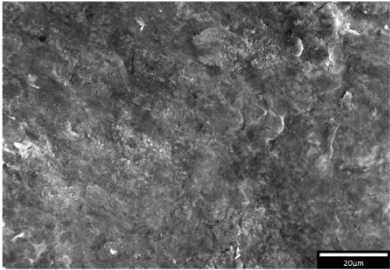
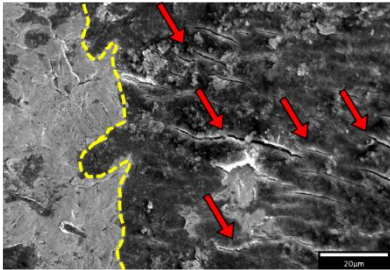
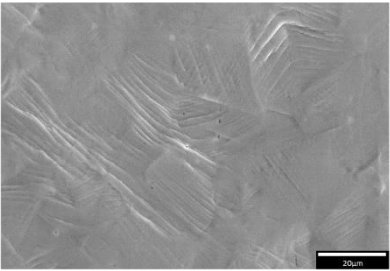
787

788

789

Figure 4 Observations of fracture surfaces a) optical microscope pictures and b) sketches with topology mapping of 1) R_{TC} polished 210 MPa, 2) R_{TC} SMAT 245 MPa,

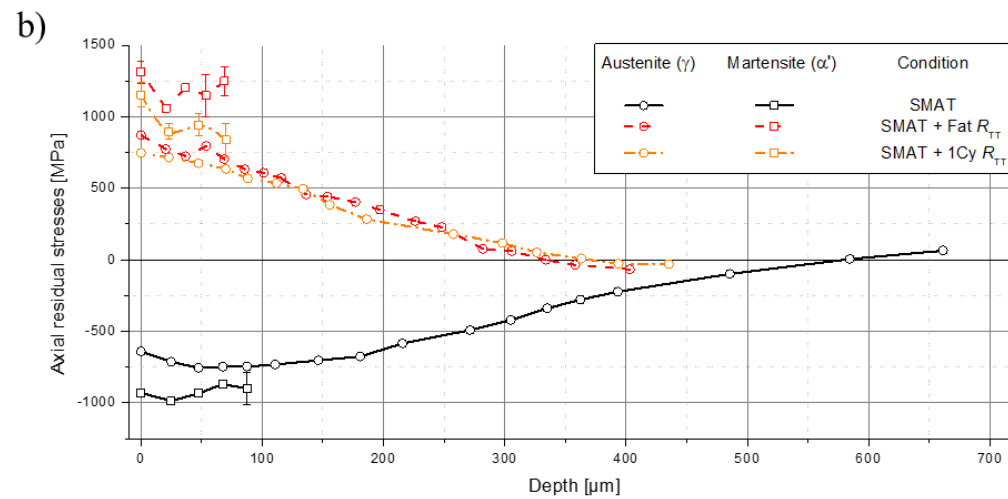
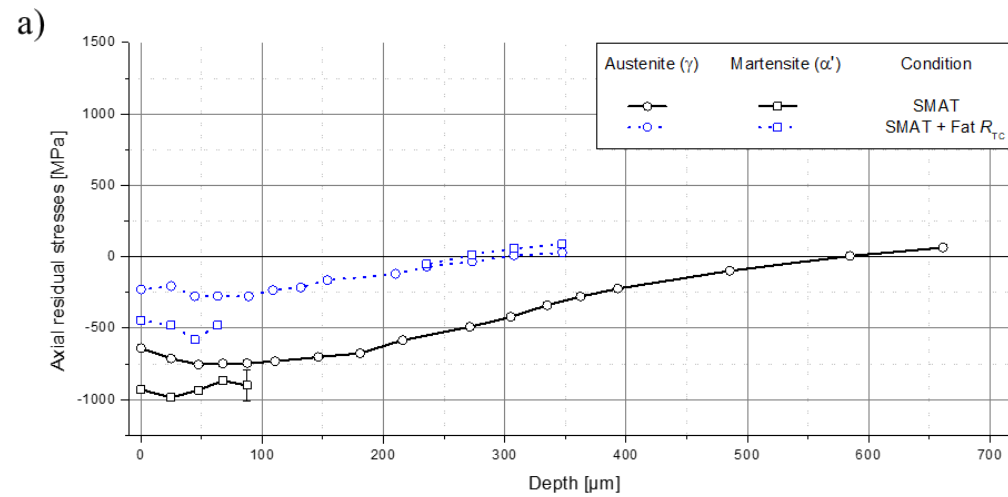
3) R_{TT} polished 232.5 MPa and 4) R_{TT} SMAT 220 MPa samples

	R_{TC}	R_{TT}
Polished	a) 	c) 
SMAT	b) 	d) 
SMAT + polished	/	e) 

790

791

Figure 5 SEM images of the surface of a) R_{TC} polished, b) R_{TC} SMAT, c) R_{TT} polished, d) R_{TT} SMAT and e) R_{TT} SMAT + polished run-out samples



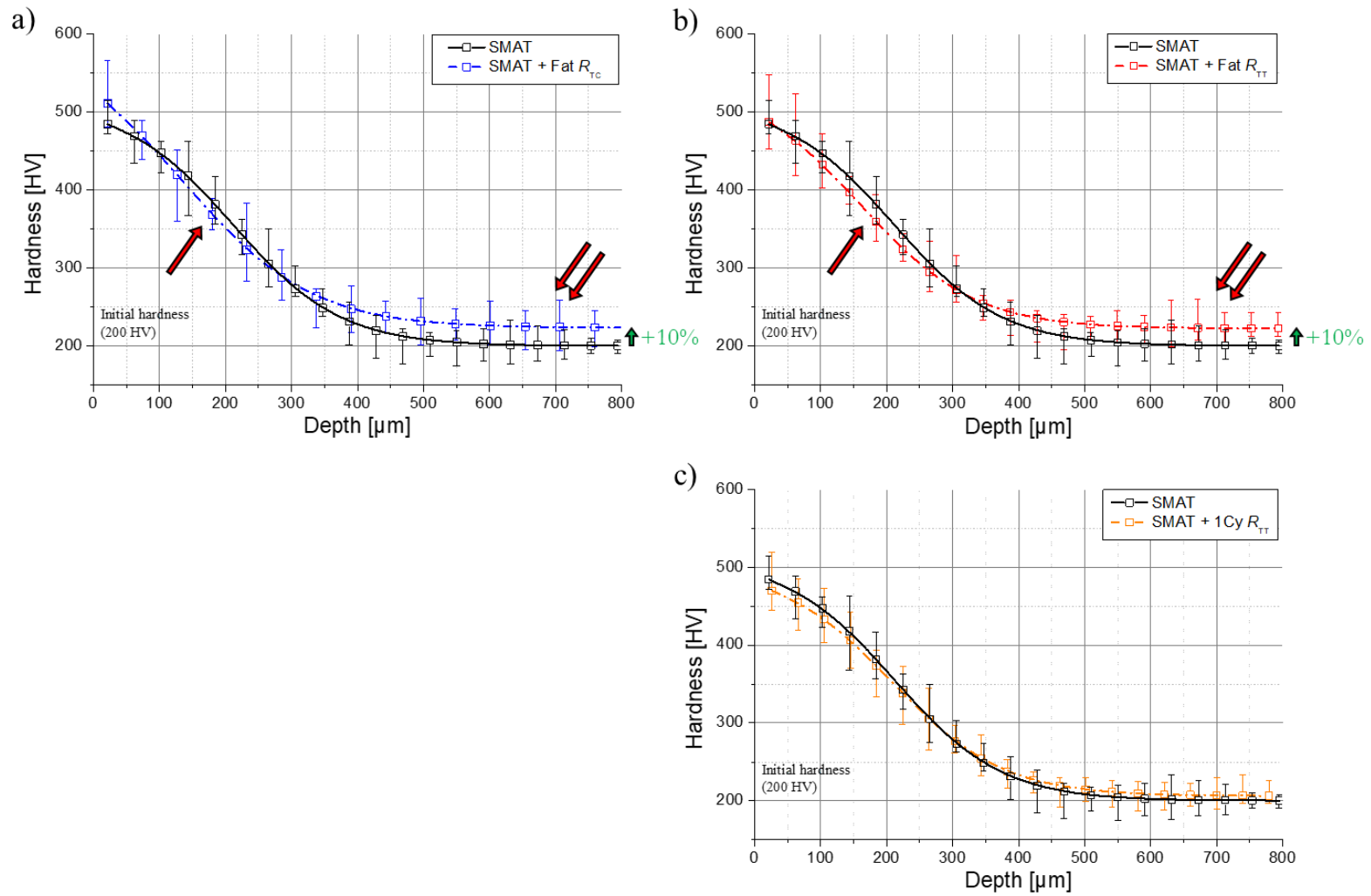
792

793

Figure 6 Evolution of the residual stresses in both austenite and martensite as a function of the depth below the treated surface a) for the SMAT + Fat R_{Tc} condition and

794

b) for the SMAT + Fat R_{TT} and SMAT + 1Cy R_{TT} , conditions compared to the SMAT gradient

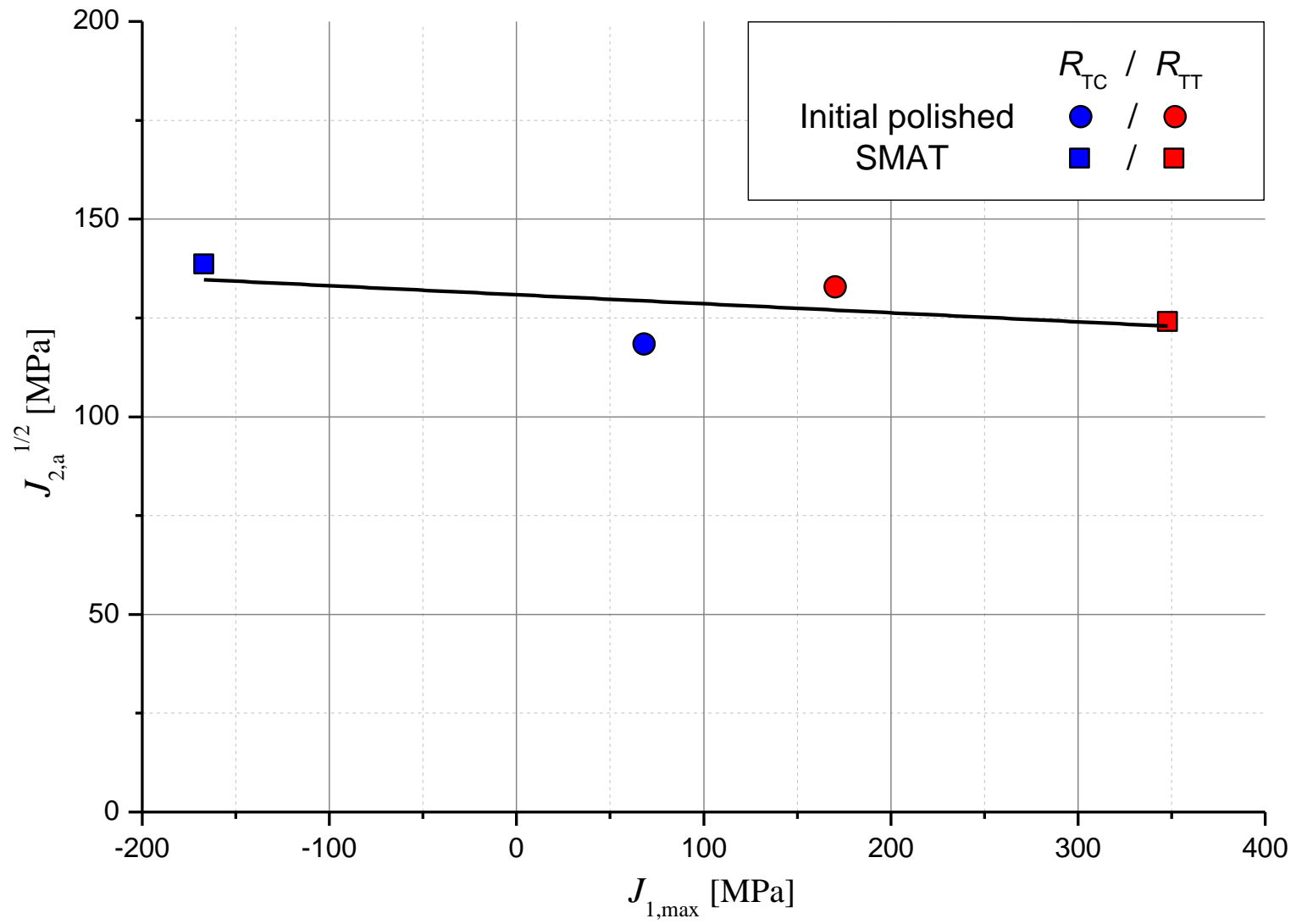


795

796 *Figure 7 Evolution of hardness as a function of the depth below the treated surface after a) SMAT + Fat R_{TC} , b) SMAT + Fat R_{TT} and c) SMAT + 1Cy R_{TT} , compared to*

797

the SMAT gradient



798

799

Figure 8 Crossland criterion established for all the tested load ratios and surface states